Activation of inorganic peroxides with magnetic graphene for the removal of antibiotics in wastewater

Rafael R. Solís[1, *], Ozge Dinc[1,2], Guodong Fang[3], Mallikarjuna N. Nadagouda[4], Dionysios D. Dionysiou[1]

[1]Environmental Engineering and Science Program, Department Chemical and Environmental Engineering, University of Cincinnati, 45221, Cincinnati, Ohio, USA

[2]Department of Biotechnology, Hamidiye Health Science Institute, University of Health Sciences-Turkey, 34668, Uskudar, Istanbul, Turkey

[3]Key Laboratory of Soil Environment and Pollution Remediation, Institute of Soil Science, Chinese Academy of Sciences, 210008, Nanjing, PR China

[4]U. S. Environmental Protection Agency, Office of Research and Development, Center for Environmental Solutions and Emergency Response, 45268, Cincinnati, Ohio, USA

*Correspondence to Rafael Rodríguez Solís (rodrigr2@ucmail.uc.edu)

Abstract

Magnetic graphene catalysts were prepared for the removal of antibiotics (sulfamethoxazole, norfloxacin, tetracycline and flumequine) in water. Different proportions of magnetite-graphene from 1:0 to 0:1 were considered to study the catalytic activation of inorganic peroxides, i.e. peroxymonosulfate (PMS), peroxydisulfate and hydrogen peroxide. The presence of graphene was mainly the responsible for the activation, which was most effective in the presence of PMS. A ratio of 20% of magnetite in the solid was enough to achieve complete degradation of antibiotics with high recovery by application of a magnetic field. The performance of the catalyst was further evaluated in a simulated urban wastewater, studying the main parameters affecting the process and the stability in sequential reuses. The non-radical mechanism during the catalytic activation of PMS was hypothesized from kinetic scavenging probes tests. The electron transfer was suggested as the mechanism of the reaction from EPR results in the presence

of D_2O. The prepared magnetic catalyst showed high catalytic activity and stability to remove antibiotics in water.

Keywords: antibiotics, inorganic peroxides, magnetic graphene, peroxymonosulfate, water treatment

1. INTRODUCTION

The pressure exerted by human activities during the last decades is pushing access to freshwater into an alarming situation. Current solutions are guided to the circular economy system, whose aim aligns with the human and natural water cycles. This strategy includes the reuse of wastewater (WW) for other applications or the safe replenishment of water basins. In this sense, the presence of different anthropogenic organic micropollutants in WW requires the development of new technologies since the current processes have been postulated as inefficient for that purpose [1,2]. These micropollutants, also known as Contaminants of Emerging Concern (CECs), include a large list of substances such as personal care products, endocrine disrupting compounds, pharmaceuticals, plasticizers, flame retardants, and other organics whose widespread use by human activities and ubiquitous presence in the environment has raised concern [3].

The removal of CECs has been widely researched through Advanced Oxidation Processes (AOPs), whose mechanism of action relies on the generation of Reactive Oxygen Species (ROS) for the oxidation of these compounds. Although AOPs based on hydroxyl radicals are effective for CECs removal [4], new techniques involve other oxidant radical species from organic peroxides [5,6], nitrogen oxide [7], or sulfate peroxides [8,9]. Peroxymonosulfate (PMS) and peroxydisulfate (PDS) can be activated by breaking their peroxide bond to trigger the formation of sulfate radicals. Diverse strategies have pursued the activation of PMS or PDS such as application of temperature, heat, radiation either ultraviolet or solar, homogeneous catalysis, or heterogeneous catalysis [9–11]. Recently, the use of carbocatalysis has emerged in the scientific community as an alternative to metallic solids in the activation of inorganic peroxides that barely can be extrapolated to a real water application, as they are expensive and/or toxic. In this sense, carbon catalysts emerge as an environmentally friendly alternative. Graphene, a hexagonal carbon plate

of few layers, is gaining attention in many applications. In water treatment, besides its attractive adsorption activities [12,13], graphene can be incorporated in environmental catalysis for different purposes. Recent works have applied carbon materials in the activation of PMS [14] and PDS [15] to generate singlet oxygen as the main species. However, the use of heterogeneous catalysts must address the recovery of the solid and reactivation if necessary, after the treatment. Therefore, diverse strategies can be considered for the recovery of nanoparticles in water treatment, such as immobilization into inert supports [16,17] or use the advantage of magnetic properties. In this sense, iron-based materials, that are magnetically active, represent a non-toxic, reasonably inexpensive, and feasible application in water treatment [18]. Diverse magnetically separable magnetite–reduced graphene oxide or graphene oxide heterojunctions have been successfully applied as nano-adsorbent [19], catalyst [20–22], and base for photocatalysts [23–25].

This work reports the synthesis and application of magnetic graphene (MG), i.e. magnetite graphene composite, for the activation of inorganic peroxides, i.e. PMS, PDS, and hydrogen peroxide, and assess their relative efficiency for the degradation of antibiotics in water. Fe_3O_4 nanoparticles at different proportions were successfully attached to graphene nanoplatelets, leading to a magnetic catalyst with low iron leaching, which makes possible the magnetic separation of the solids from the aqueous solution. Different techniques were used to characterize the surface and properties of the catalysts (N_2 adsorption, SEM, TEM, FTIR, Raman, XRD, XPS, Quantum Design PPMS® DynaCool™). The solid was catalytically active for PMS>PDS>H_2O_2 applied to the removal of sulfamethoxazole as the target compound. The efficiency of PMS+MG was also assessed for other antibiotics (norfloxacin, tetracycline, and flumequine) and under a more realistic scenario by using simulated urban wastewater (SUWW). A deeper analysis of the influence of process parameters (i.e. dose of the catalyst, initial PMS

concentration, pH, reusability) was carried out in the SUWW. The non-radical mechanism of the catalytic activation of PMS was elucidated by scavenging probe tests and corroborated by EPR. Moreover, this technique provided evidence to support the electron transfer mechanism from the organic to the PMS mediated on the surface of the magnetic graphene catalyst.

2. EXPERIMENTAL

2.1. Chemicals

Sulfamethoxazole (SMX, $C_{10}H_{11}N_3O_3S$, CAS: 723-46-6, TCI® America), norfloxacin (NFX, $C_{16}H_{18}FN_3O_3$, CAS: 70458-96-7, Alfa Aesar®), tetracycline (TCL, $C_{22}H_{24}N_2O_8C$, CAS: 60-54-8, Alfa Aesar®), and flumequine (FLU, $C_{14}H_{12}FNO_3$, CAS: 42835-25-6, Alfa Aesar®) were of analytical grade (>98%).

For magnetic graphene synthesis, graphene nanoplatelet aggregates (500 $m^2\ g^{-1}$) were acquired from Alfa Aesar® while analytical grade $FeSO_4 \cdot 7H_2O$ and $FeCl_3 \cdot 6H_2O$ were purchased from Sigma Aldrich®.

The oxidant used was Oxone® (Sigma Aldrich®) as peroxymonosulfate (PMS) source, potassium persulfate (Fisher®) as peroxydisulfate (PDS), and hydrogen peroxide (Acros Organics®).

The simulated urban wastewater (SUWW) was prepared following the recipe proposed by Erdei et al. [26] with chemicals from Sigma-Aldrich®. Table 1 shows the chemical composition of the SUWW matrix (final pH=9.5).

Table 1. Chemical composition of the simulated urban wastewater (SUWW)

Chemical compound	C (mg L^{-1})
Beef extract	1.8
Peptone	2.7
Humic acid sodium salt	4.2
Tannic acid	4.2
Sodium lignin sulfonate	2.4
Sodium lauryl sulfate	0.94
Acacia gum powder	4.7
$(NH_4)_2SO_4$	71

K_2HPO_4	7.0
NH_4HCO_3	19.8
Na_2SO_4	0.71

The rest of the chemicals were of analytical grade and were used without further purification. All solutions were prepared with ultrapure water produced from a Barnstead™ E-Pure™ device (resistivity > 17.5 MΩ·cm). HPLC grade acetonitrile (Fisher®) was used for liquid chromatography analyses.

2.2. Experimental procedure

Degradation tests were carried out in magnetically stirred beakers of 250 mL. Target organic micropollutants were dissolved in ultrapure water or SUWW matrix depending on the experiment. Reaction tests started by adding simultaneously inorganic peroxides (PMS, PDS, or H_2O_2) from a concentrated solution (generally 0.1 M) and graphene to the solution that already contained the target organic micropollutant. For comparison purposes, adsorption experiments were conducted without oxidant addition. The direct oxidation by the corresponding inorganic peroxides was also tested individually. Samples at different times were extracted, filtered with nylon syringe filters (Simplepure™, 0.45 μm), and quenched with sodium thiosulfate before HPLC analysis. Assays with control of pH were conducted by adding 5 mM of H_3PO_4 and/or concentrated NaOH until reaching the desired value. The catalysts were magnetically recovered, when necessary, with the help of a magnet and dried at 80 ºC overnight.

2.3. Aqueous analyses

The aqueous concentrations of the model micropollutants were analyzed by liquid chromatography (Agilent 1100 HPLC) equipped with DAD detector. For the separation, a Discovery® HS C18 column (15x4.6 mm, 5 μm, Supelco®) was used as the stationary phase. A mixture of acetonitrile (A) and acidified ultrapure water (0.05% trifluoroacetic acid, B) was pumped at a rate of 1 mL min^{-1}. A proportion A:B=30:70 was used for the

125 analysis of sulfamethoxazole, norfloxacin, and tetracycline; while for flumequine a ratio
126 of 40:60 was used. The quantification was conducted at 220 nm for flumequine, 286 nm
127 for norfloxacin, and 260 for sulfamethoxazole and tetracycline.

128 The concentrations of peroxymonosulfate and peroxydisulfate were analyzed
129 colorimetrically by DPD (*N,N*-diethyl-*p*-phenylenediamine) oxidation at buffered media
130 [27]. Hydrogen peroxide concentration was also spectrophotometrically quantified by
131 complexation with titanium (IV) oxysulfate [28].

132 The total iron dissolved was analyzed by reduction of all iron species to iron (II) and
133 complexation with 1,10-phenanthroline (FerroVer® iron reagent, Hach®).

134 The reactive oxidant species involved in the catalytic activation were identified with
135 Electron Paramagnetic Resonance (Bruker E500 spectrometer, Germany). The presence
136 of $^1O_2$ or the electron transfer mediated reaction was detected by adding TEMP (4-amino-
137 2,2,6,6- tetramethylpiperidine) as a spin-trapping agent and by comparing the results in
138 H_2O and D_2O solutions. DMPO (5,5-dimethyl-1-pyrroline-N-oxide) was used as a spin-
139 trapping agent for the detection of radicals, i.e. $O_2^{\bullet-}$, $HO^{\bullet}$ and $SO_4^{\bullet-}$.

140 **2.4. Catalyst synthesis and characterization**

141 Magnetic graphene was prepared following the co-precipitation of ferrous and ferric
142 salts at alkaline media [29]. Briefly, a fixed amount of commercial graphene was placed in
143 200 mL of ultrapure water in which $FeCl_3 \cdot 6H_2O$ and $FeSO_4 \cdot 7H_2O$ were previously
144 dissolved with a molar ratio Fe^{3+}/Fe^{2+}=2.45, according to the proposal of Petcharoen and
145 Sirivat [30]. The pH was raised until reaching a value of 9 by the addition of concentrated
146 ammonium hydroxide. The precipitated solid was separated with the help of a magnet.
147 Thereafter, the solid was washed several times with ultrapure water and dried at 80 ºC.
148 The catalysts were labeled as MGX where X means the weight ratio of magnetite
149 nanoparticles in the solid.

Nitrogen adsorption isotherms were carried out to quantify the surface area and to evaluate the porous properties of the MG solids. The device used was a Micromeritics® Tristar 3000 (-196 ºC, specific surface area resolution 0.01 m^2 g^{-1}). The degasification of the samples was carried out in the 24 h before the analysis (120 ºC, N_2 as purging agent).

Imaging of morphology, shape, and size of nanoparticles was conducted in a Thermo Scientific™ Scios™ DualBeam™ Scanning Electron Microcopy (SEM), equipped with surface Energy Dispersive X-ray (EDX) elemental analysis. Solid samples were dispersed in 2-propanol and dropped on a copper grid. Alcohol was naturally dried before the image depicting. Imaging at higher amplification was carried out in a JEM-2100F Transmission Electron Microscopy (TEM) device (JEOL, Japan) at an acceleration voltage of 200 kV, equipped with Energy-Dispersive X-ray (EDAX) analysis.

Fourier Transform InfraRed (FTIR) was used to study the surface functional groups in an Agilent® Cary 600 series FTIR spectrometer.

The disorder of graphene structure was studied using Raman spectroscopy in an inVia™ Qontor® Raman microscope from Renishaw©. Spectra were recorded using a laser beam of 633 nm.

The crystalline composition was studied employing X-Ray Diffraction in a Panalytical (Expert) 2-theta diffractometer. The device used monochromatic CuKα radiation (1.54 Å) and the angle range (2θ) was recorded within 2 and 90°. The phase identification from powder diffraction was carried out with *Match!*© software.

The surface oxidation states of oxygen, carbon, and iron were studied in a PHI VersaProbe III X-ray Photoelectron Spectroscopy (XPS) microprobe instrument with Kα Al monochromatic radiation (1486.68 eV).

The magnetization behavior (magnetic susceptibility, M_S) of the nanoparticles was measured in a Quantum Design PPMS® DynaCool™ device under Vibrating Sample

175 Magnetometer (VSM) option at room temperature applying an external magnetic field
176 (H) within $\pm 3 \cdot 10^4$ Oe.

177 **3. RESULTS AND DISCUSSION**

178 **3.1. Characterization of the material**

179 The surface textural properties of the MGX catalysts were assessed by N_2 adsorption-
180 desorption isotherms. Table 2 shows the specific surface area obtained by the Brunauer-
181 Emmett-Teller (BET) method. Magnetite nanoparticles displayed a low value of the
182 specific surface area, 66 $m^2 g^{-1}$. A larger value was obtained for raw graphene, 494 $m^2 g^{-1}$
183 which is close to the value of 500 $m^2 g^{-1}$ suggested by the manufacturer. The magnetic
184 graphene solids presented a proportional area according to their composition of magnetite
185 and graphene. Magnetite, due to their nanoparticle structure showed more percentage of
186 micropores. Although the addition of graphene resulted in a higher surface area, the nature
187 of this porosity is due to meso and macropores.

188 **Table 2.** Characterization results of the magnetic-graphene catalysts

Catalyst	C percentage (mass)	N_2 adsorption-desorption isotherms		Atomic surface Composition (%)			Oxygenated bonds in O1s region (%)			M_S (emu g^{-1})
		BET area (m^2 g^{-1})	Micropores (%)	C	O	Fe	C-O	Fe-O-C	Fe-O	
Graphene	100	494±3	21.4	96.23	3.77	-	37.2	-	-	n.m.
MG0.2	77.2	361±2	20.3	92.93	6.53	0.54	23.6	41.2	35.2	1.41
MG0.4	61.5	281±2	23.3	90.20	8.88	0.97	21.2	36.1	42.7	12.7
MG0.6	36.0	244±1	11.5	85.78	12.39	1.83	21.4	24.2	54.4	32.6
MG0.8	22.3	194±2	32.0	84.26	13.29	2.44	13.7	29.4	52.7	48.1
Magnetite	0	66±1	69.2	-	82.30	17.70	-	-	100	55.9

189

The morphology and composition of the catalysts were studied by Scanning Electron Microscopy (SEM) with Energy Dispersive Analysis of X-ray (EDAX). Fig. 1 depicts images for bare magnetite nanoparticles, bare graphene nanoplatelets, and the magnetic graphene MG0.2. For the rest of magnetite: graphene ratios more images are available in the supplementary information (Fig. S1). Raw magnetite consisted of an aggregation of almost sphere-shaped nanosized particles, aggregated between them due to magnetic dipole interactions. Bare graphene nanoparticles (Fig. 1B) can be described as an agglomeration of wrinkled sheets of different sizes and shapes. Typical nanoplatelets of 500 nm size were frequently observed (Fig. 1B1). The addition of magnetite to graphene resulted in small semi-spherical magnetite particles adhered to the carbon nanoplatelets. Also, MG0.2 and MG0.4 (see in Fig. S1) simultaneously displayed some nanorods. The presence of these nanorods suggests the formation of other undesirable iron species alternative to magnetite. These nanorods can be attributed to the oxyhydroxide goethite (α-FeOOH), which is usually formed in the co-precipitation of iron (II) and (III) salts [31], as it proved later on with XRD analysis.

To justify the presence of iron in the sample MG0.2, EDAX mapping was conducted (Fig. 1 D) confirming that the shiny small quasi-spherical particles observed correspond to iron particles (red-colored, subfigure D3). Moreover, from the mapping for carbon and oxygen (blue and green colored regions, see subfigures D1 and D2 respectively), it is concluded that graphene nanoplatelets are not oxygenated as the oxygen mapping perfectly overlaps only the iron colored regions. It is also observed that the incorporation of magnetite nanoparticles prevented the aggregation of the catalytic nanoparticles with some interspaces among them, which exerts a positive effect when dispersed into solution.

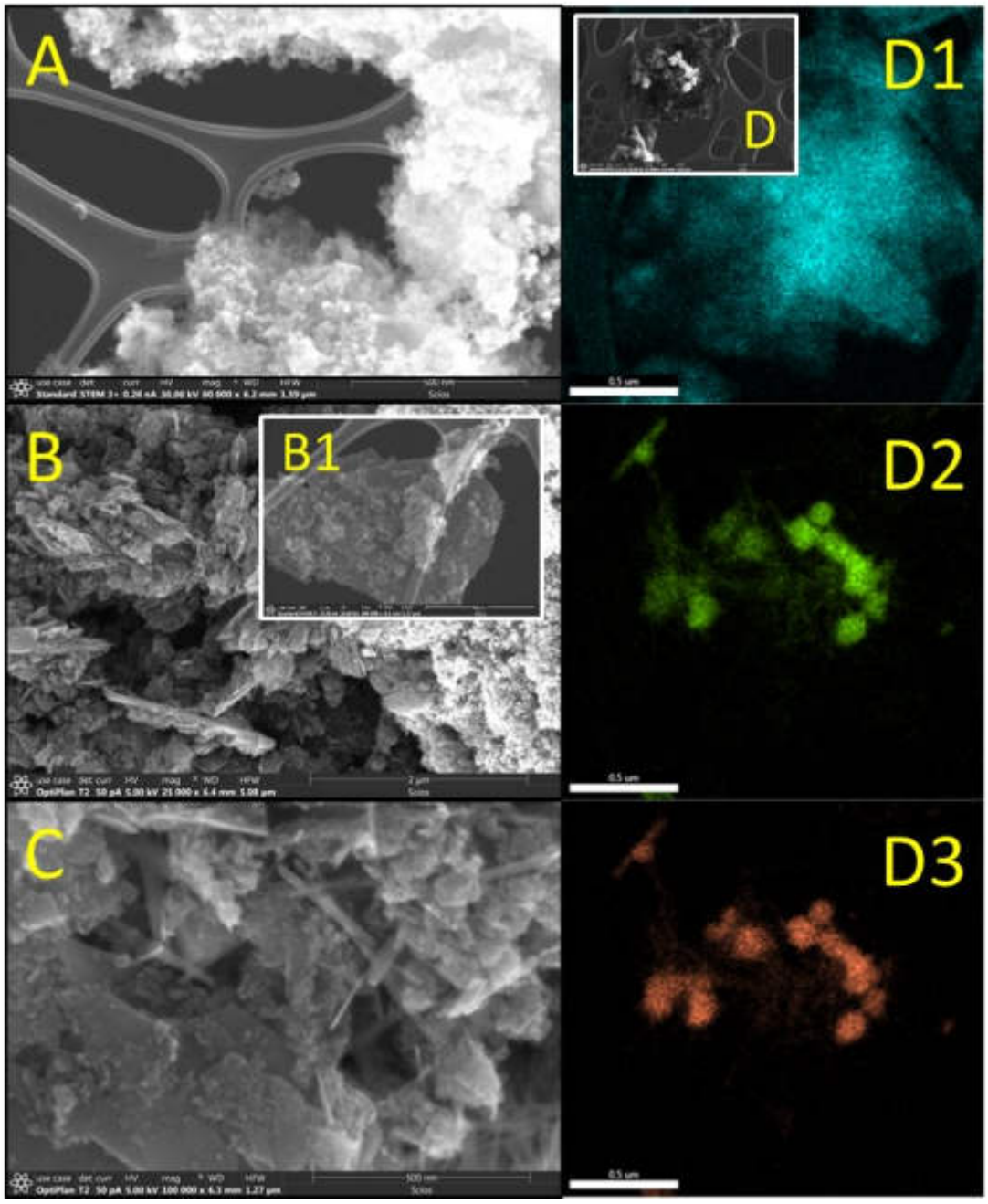

Figure 1. SEM micrographs of bare magnetite (A), bare graphene (B and B1), and MG0.2 magnetic graphene (C). EDAX mapping of carbon (D1), oxygen (D2), and iron (D3) in sample MG0.2 (D).

The presence of magnetite was further confirmed by TEM analysis. The presence of magnetite nanoparticles onto thin graphene nanosheets was observed in TEM imaging, see as an example the TEM micrographs took for MG0.2 in Fig. 2A. Also, the EDAX mapping allowed to confirm the presence of iron in the dark particles and carbon in the

nanosheets (Fig. 2B and B1). Further analysis of Selected Area Electron Diffraction (SAED) onto the iron nanoparticles led to the depicting of magnetite SAED pattern, see Fig. 2 C. Moreover, the analysis of the composition by EDAX of the sample MG0.2 revealed 15.3 % of Fe_3O_4 and 86.6% of carbon.

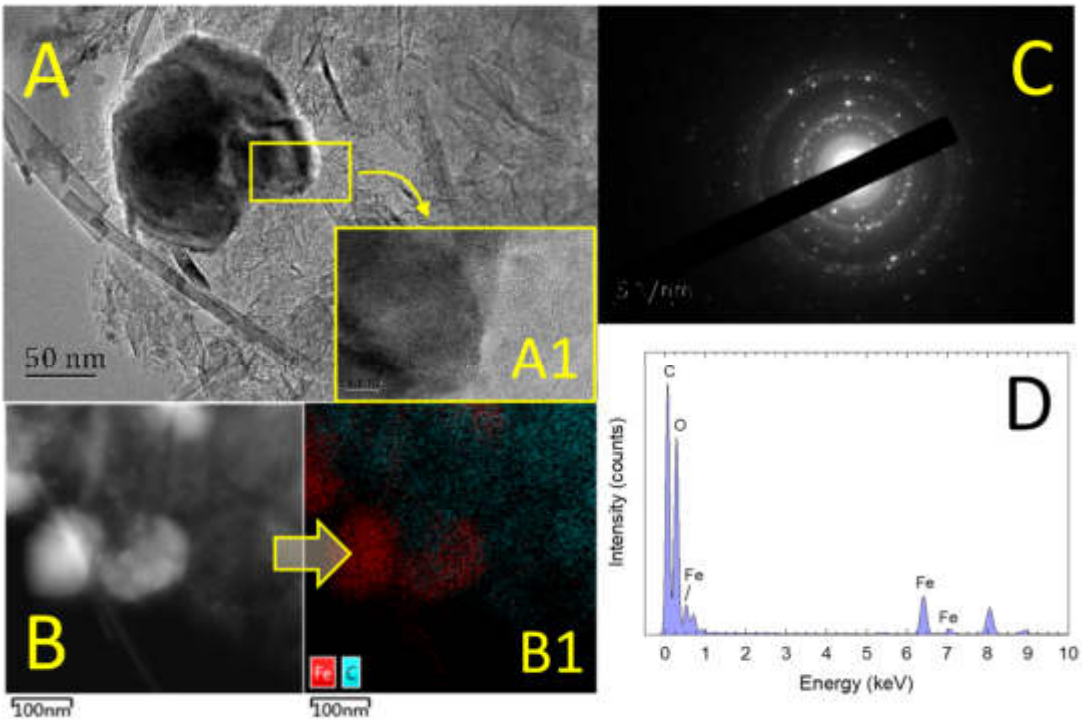

Figure 2. TEM micrographs of MG0.2 sample. (A) and (A1) TEM images at different magnifications; (B) and (B1) EDAX mapping analysis with C Kα (blue) and Fe Kα (red); (C) SAED pattern of magnetite; (D) EDAX spectrum.

The presence of magnetite and graphene was confirmed by analyzing the crystalline composition with X-Ray Diffraction (XRD) technique (see Fig. 3). Reduced graphene presented a characteristic peak at 26.4º attributed to the hexagonal of graphitic carbon. Bare magnetite is characterized by a mean peak located at 35.5º and minor peaks located at 30.2º, 57.2º, 62.2º, and 75.3º. Magnetic graphene displayed peaks of graphene and magnetite proportionally to the relative carbon-iron composition. In the case of the minor iron proportion, i.e. MG0.2 and MG0.4, residual presence of the oxyhydroxide goethite (α-FeOOH) was confirmed (major peak located at 21.4º and minor peaks at 33.3º and

238 36.7º). A high proportion of reduced graphene in the synthesis process promoted the
239 formation of this species. On the contrary, high amounts of graphene resulted positively
240 to keep a reductive environment for the formation of magnetite [32]. This result suggests
241 that the nanorods appreciated in SEM images of MG0.2 and MG0.4 samples are goethite.

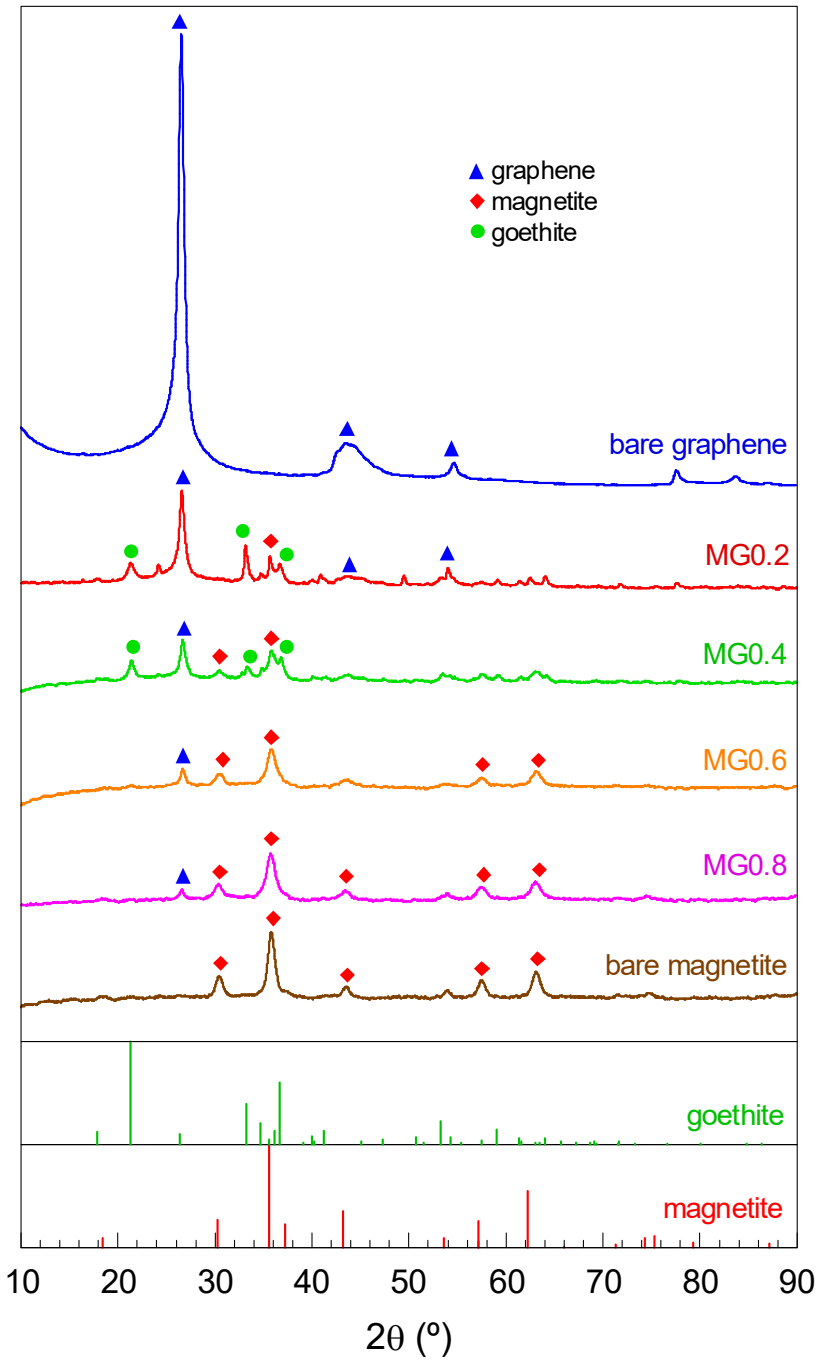

242

243 **Figure 3.** XRD patterns of magnetic graphene with different magnetite ratios

244 FTIR spectra showed a lack of oxygenated functional groups on carbon lattice (Fig.
245 S2) or hydroxylated groups as previously suggested SEM-EDAX mapping. Only bare
246 magnetite presented a wide band at about 3400 cm^{-1} attributed to the surface –OH groups.

247 Raman spectroscopy is a powerful technique to study the disorder of the hexagonal
248 honeycomb of graphene materials. Raman spectra of graphene in Fig. S3 is characterized
249 by three peaks, D peak at around 1330 cm^{-1}, G peak located at ca. 1570 $cm^{-1,}$ and a 2D
250 band whose maximum was placed at 2650 cm^{-1}. D peak defines the disorder on the
251 hexagonal carbon, G peak is characteristic of the sp^2 carbon aromatic bonds common in
252 graphitic structures, and the second-order 2D band appears in detriment of D peak when
253 the material presents high order, and therefore a low proportion of sp^2 amorphous carbon
254 [33]. Monolayer graphene is characterized by a sharp and tiny 2D peak [34]. Magnetite is
255 characterized by a low-intensity peak located at around 670 cm^{-1}. As can be observed in
256 Fig. 4, the 2D band peak losses intensity as the proportion of magnetite in the solid
257 increases. This indicates that the disorder in the graphene structure is higher due to the
258 greater presence of magnetite nanoparticles. In this sense, an analysis of the relative
259 proportion of D and 2D intensity confirms that fact. However, the G peak in bare graphene
260 presents a shoulder which is the consequence of the overlapping of D' peak [35], which
261 appears with a high proportion of sp^3 hybridization or the presence of vacancies in the
262 hexagonal sheet of graphene [36]. This shoulder is less appreciable as the amount of
263 magnetite is raised in the solid. The peak of magnetite at 670 cm^{-1} is only appreciated in
264 the samples with the highest content of magnetite (MG0.6 and MG0.8), due to the low-
265 intensity contribution of this peak if compared to the peaks coming from graphene
266 structure.

267 The surface chemical composition was studied by X-ray Electron Spectroscopy (XPS).
268 This technique not only gives information about the chemical composition in the surface

but also about the oxidation states of the elements and the nature of oxidation groups on the surface. High-resolution spectra of the O1s, C1s, and $Fe2p_{2/3}$ regions and their respective deconvolution of the magnetic graphene catalysts are available in the supplementary material (Fig. S4). For comparison purposes, graphene and magnetite nanoparticles were also analyzed by XPS. The raw graphene presented a low proportion of surface oxygenated groups, 3.77% of atomic O, mainly composed of C=O and C-O groups. The chemical interaction between magnetite and graphene has been postulated by two different bonds: a possible connection between Fe and carbon with oxygen as a bridge (Fe-O-C) or direct bond Fe-C. From the high-resolution spectra of C1s, the possibility of Fe-C bond is excluded since no peak at 283.3 eV was registered [37,38]. The C1s peak denoted the existence of non-oxygenated aromatic carbon bonds (284.6 eV). The oxygenated groups observed in the C1s region were C-O and O-C=O. The presence of Fe_3O_4 was corroborated by the $Fe2p_{3/2}$ high-resolution spectra in which the two oxidation states of iron, Fe^{2+}, and Fe^{3+}, were identified [39]. The existence of a possible Fe-C bond was also discarded in these spectra. From O1s spectra, the formation of Fe-O and Fe-O-C bonds was suggested. Moreover, as the magnetite percentage was raised, the percentage of oxygen increased accordingly. Likewise, the Fe-O bounding percentage increased to the detriment of C-O and Fe-O-C groups due to a lesser amount of carbon in the sample (see Table 2 and Fig. S4). For comparison purposes, the global carbon percentage was quantified by calcination of the solids at 500 ºC.

The magnetic properties of the prepared MGX catalysts were analyzed by measuring magnetization dipole moment (M) *versus* the applied magnetic field (H) to estimate the saturation magnetic moment (M_S). Fig. 4A depicts the results of M-H curves and Fig. 4B illustrates the influence of the presence of magnetite in the M_S value (also see Table 2). As expected, an increase in the M_S was registered as the percentage of iron in the catalyst

was raised. For the MG1.0 sample, a value of 55.9 emu g^{-1} was obtained, which matches the 60-90 emu g^{-1} values usually reported for magnetite nanoparticles depending on the particle size, distribution, and possible oxidation of magnetite nanoparticles to less magnetic maghemite during the synthesis process [40,41]. No maghemite formation was detected in XRD patterns for MG1.0. The rest of the catalysts showed proportionally less M_S according to their magnetite content. However, this proportionality was inferior to the expected contribution considering that firstly, the M_S value obtained for bare magnetite; and secondly, that all the iron in the samples is accounting as magnetite (see Fig. 4B). The formation of oxyhydroxide goethite (α-FeOOH) as proved in SEM-EDAX and XRD techniques would explain this loss in M_S values, especially for MG0.2 and MG0.4. The lowest M_S = 1.41 emu g^{-1}, recorded for MG0.2, is still comparable to the magnetic saturation moment reported for other similar iron catalysts in water treatment application [24,42,43]. Moreover, it allows the physical separation aided with the application of an external field.

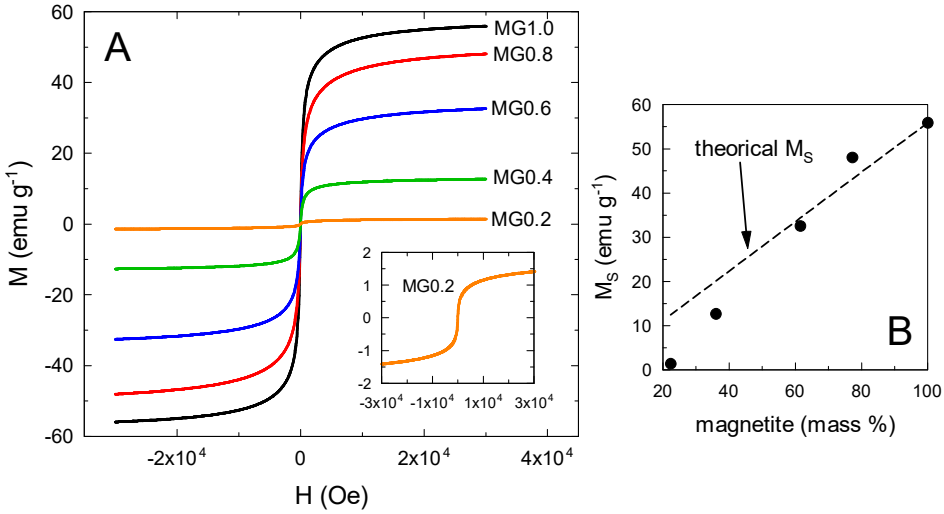

Figure 4. Magnetic properties of MGX catalysts. A, Magnetization moment (M) *vs* the magnetic field applied (H) for the different MGX magnetic catalysts (MG0.2 for inlet subfigure). B, Influence of magnetite proportion in the saturation magnetization moment (M_S).

313 The stability of the MGX catalysts in ultrapure water was assessed at different pH
314 values by analyzing the leached iron into the aqueous solution. Fig. S5 depicts the amount
315 of the released total iron in aqueous solution per amount of catalyst after 120 min. The
316 evolution of iron over time is available in Fig. S6. It was observed that the higher the
317 amount of iron in the solid, the higher the iron leaching observed, especially for MG0.6
318 and MG0.8. In contrast, MG0.2 and MG0.4 solids did not release significant amounts of
319 iron and their use in water solution does not mean a hazard in terms of metal leaching.
320 Regarding the pH influence, the higher amount of iron was released at pH 7 and 9 for the
321 catalyst with the highest proportion of magnetite (MG0.6 and MG0.8). The presence of
322 graphene has been reported to minimize the iron leaching observed at acid pH in
323 magnetite [44]. However, those catalysts with less amount of graphene (MG0.6 and MG0.8)
324 demonstrated lower stability and higher leaching at basic pH. Furthermore, for the
325 evolution of these pH values with time, a decrease of the iron concentration in solution
326 was registered with time (see Fig. S6). This decrease of iron can be attributed to the
327 adsorption of iron cations onto the graphene surface.

328 **3.2. Catalytic activity for the activation of different inorganic peroxides**

329 *3.2.1. Catalytic activity. Influence of magnetite: graphene ratio*

330 The contribution of graphene and magnetite to the catalytic activation of PMS, PS, and
331 hydrogen peroxide was first studied using sulfamethoxazole (SMX) as a target model
332 micropollutant. Fig. 5 depicts the temporal evolution of the normalized concentration of
333 SMX for the different systems and magnetite: graphene ratios. Adsorption experiments
334 were also accomplished for comparison purposes.

335 As shown in Fig. 5A, the bare graphene presented a moderate removal of SMX by
336 adsorption (over 45% in 2h) while magnetite nanoparticles did not show any adsorption

activity. Intermediate ratios of magnetite, 20 to 60% led to almost 20% of SMX removal. The solid MG0.8 did not exhibit significant adsorption capacity.

The direct reaction of SMX with H_2O_2, PDS, or PMS was also studied. As observed in the respective Figs. 7B to D, the oxidation was negligible in the case of H_2O_2 or PDS, and moderate with PMS (30% in 2h). PMS is expected to attack electron-rich regions such as aromatic rings and double bonds as reported in diverse examples in the literature [45–47]. In the case of sulfonamides, electrophilic oxidation of $–NH_2$ to $–NO_2$ and nucleophilic attack to S atom have been reported in the literature [46]. The reaction of SMX and PMS presents a second-order rate constant in between 0.05-0.23 M^{-1} s^{-1}, depending on the pH [47]. The simulation of the evolution of SMX with the reported rate constant under the conditions applied here fits well the experimental data obtained (see the dashed grey line in Fig. 5B).

The combination of PMS or PDS and magnetic graphene improved in all cases the removal of SMX registered during the respective processes in the absence of the oxidant (adsorption). As shown in Fig. 5B to D, PMS was the most efficient when combining with the magnetic catalysts, followed by PDS with a moderate removal rate and H_2O_2 was the least active. The low effectiveness of hydrogen peroxide if compared to PMS has been also reported by Peng et al. [48]. In the specific case of MG0.2, which presented the highest activity of all the magnetic catalysts with considerably magnetic separation, the addition of PMS, PDS, and H_2O_2 led to SMX removal percentages of, 86, 73, and 34% (17% of adsorption, blank test in absence of catalyst) respectively after 2h. In the case of PMS, if the action of direct reaction is eliminated (30% in 2h), the activities of PMS and PS after 2 hours are similar. However, from the higher slopes of the normalized curves of temporal concentration, a higher reaction rate is obtained in the case of PMS.

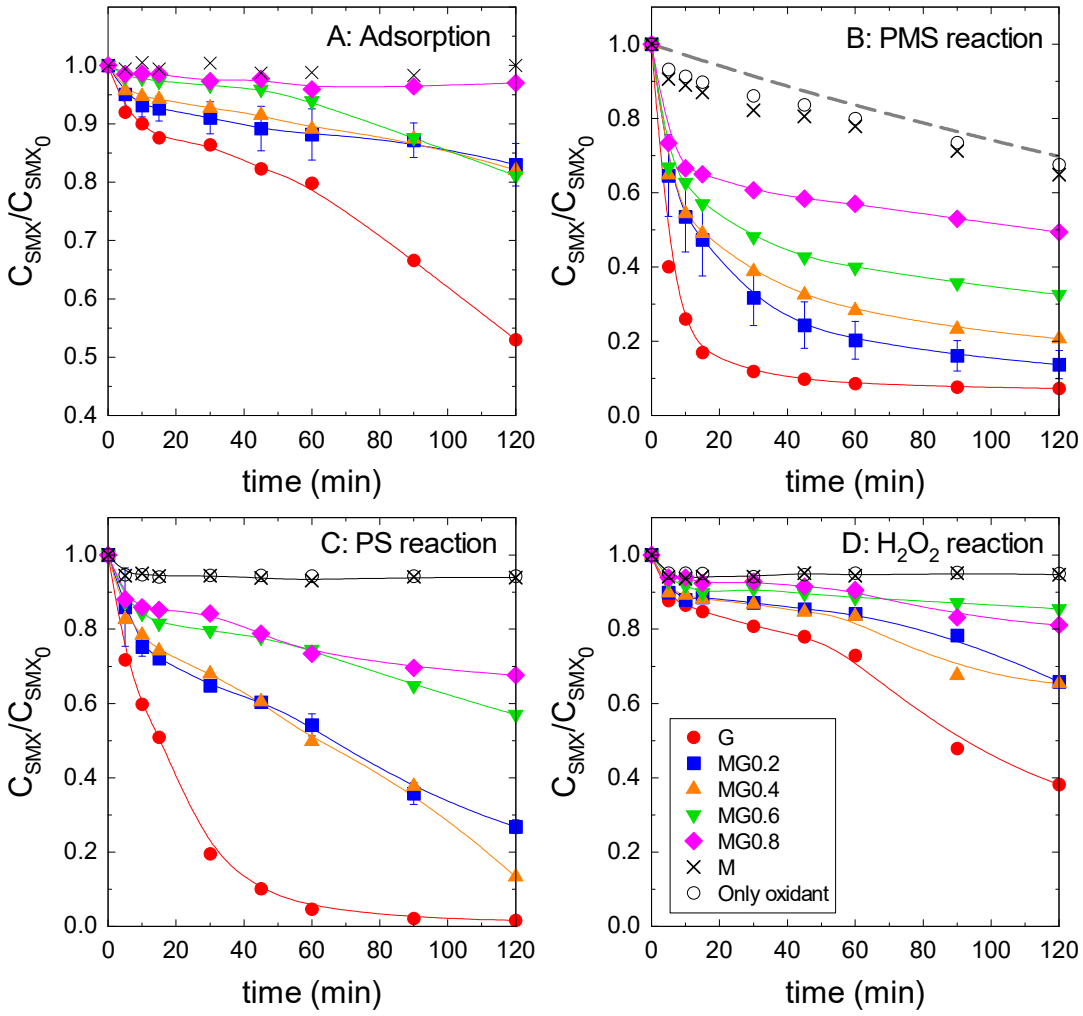

Figure 5. Oxidation of sulfamethoxazole (SMX) by catalytic activation of different inorganic peroxides (PMS, PS, and hydrogen peroxide) with magnetic graphene. Influence of magnetite: graphene ratio and oxidant nature. *Experimental conditions: V=250 mL; $C_{SMX,0}$= 5 mg L^{-1}; $C_{catalyst}$= 50 mg L^{-1}; $C_{oxidant}$=0.5 mM. Dashed grey line, simulation of SMX decay by PMS direct reaction with the rate constant available in literature* [47].

The initial rate of SMX removal ($r_{SMX,0}$, reaction rate at time zero) was calculated from the slope of the temporal SMX curve at time zero and assessed as a tool to compare the efficiency of the different catalytic systems. Thus, Fig. 6A depicts the evolution of the $r_{SMX,0}$ with the amount of graphene in each solid. As can be observed, magnetite presents a poor catalytic effect in the activation of either PMS, PS, or hydrogen peroxide. Similarly, adsorption onto magnetite nanoparticles is negligible. However, the presence

374 of graphene in the material considerably increased $r_{SMX,0}$. A catalytic effect, due to
375 graphene nanoparticles, can be envisaged if results of $r_{SMX,0}$ in the presence and absence
376 (adsorption) of oxidant are analyzed. Moreover, the selection of the oxidant in the process
377 plays an important role in SMX elimination. Hydrogen peroxide barely improved the
378 results registered during the adsorption process. Although it has been reported the H_2O_2
379 catalysis with Fe_3O_4-graphene oxide composites can achieve degradation of dyes such as
380 acid orange 7 [49] or methylene blue [50], the low concentration of H_2O_2 and catalyst dose
381 used in this study may explain why the catalytic effect is negligible. PDS significantly
382 accelerated the reaction but not as PMS did. The combination of PDS and Fe_3O_4-graphene
383 based materials, either rGO and GO, leads also to a catalytic effect for the degradation of
384 chlorinated micropollutants such as 2,4-dichlorophenol [21] or thricholoroethylene [51].
385 However, when PDS and PMS were compared, over double $r_{SMX,0}$ was observed in the
386 case of PMS than in the case of PDS addition. In addition, the use of PDS implies the
387 release of double sulfate amount if compared to PMS. Furthermore, the analysis of
388 peroxide conversion can better reflect the performance of catalyst. The effectiveness of
389 the catalytic activation at different magnetite-graphene proportion was also analyzed in
390 terms of peroxide consumption after 2 hours, as depicted in Fig. 6B. Also, Fig. 6C shows
391 the temporal evolution of MG0.2 as an example. It is observed that PMS is consumed at
392 a higher extent than PS or H_2O_2 in all catalysts systems tested. Besides, it is also
393 confirmed that the higher the graphene proportion is, the higher the PMS conversion is.
394 Maximum PMS conversion was displayed by raw graphene. This value gradually
395 decreased as the magnetite proportion was increased.

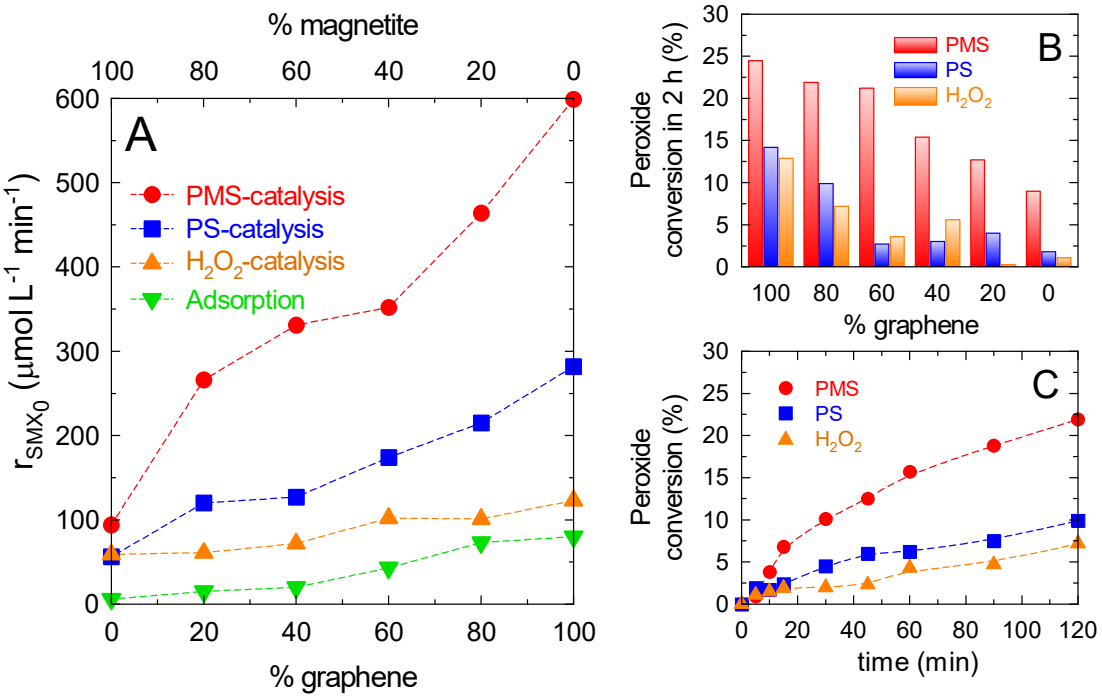

Figure 6. (A) Influence of magnetite-graphene ratio in the initial rate of sulfamethoxazole degradation during the activation of inorganic peroxides with magnetic graphene. (B) Influence of the magnetite-graphene ratio in the consumed peroxides after 2 h. (C) Temporal evolution of peroxide conversion in the catalyst MG0.2. *Experimental conditions as shown in Fig. 5.*

Although magnetite nanoparticles have been reported as catalytically active for the production of radicals when combined with H_2O_2 [52–56], PDS [53,57–59] or PMS [60,61]; the $r_{SMX,0}$ values for the prepared magnetite were lower at the catalyst dose applied (50 mg L^{-1}). Hence, the catalytic activity can be attributed to the presence of graphene nanoparticles in the material, which is thought to take place through the non-radical activation [14,62]. Nevertheless, the presence of magnetite makes the material easily recoverable by the application of an external magnetic field. There is, therefore, a compromise between the magnetite and graphene proportion in terms of recovery and catalytic activity, respectively. The solid MG0.2 was chosen for further study as it has enough magnetic properties to be separated from the treated water and the highest activity of all the magnetic catalysts tested.

413 *3.2.2. Catalytic activity of MG0.2. Influence of micropollutant nature*

414 The graphene catalyst containing 20% of magnetite (MG0.2) was further assessed for
415 the removal of the other three antibiotics, i.e. norfloxacin, tetracycline, and flumequine
416 of different nature to sulfamethoxazole. The application of the three oxidants, H_2O_2, PDS,
417 and PMS was tested in individual experiments.

418 In the case of norfloxacin (Fig. 7A), no significant reaction with PDS or H_2O_2 was
419 observed; nevertheless, as in the same way as SMX, partial oxidation was registered with
420 PMS. The PMS-catalytic system was the most efficient, 95% norfloxacin removal in 2 h.
421 PDS or H_2O_2 barely improved the results registered with adsorption, 40% of elimination
422 in 2 h.

423 As shown in Fig. 7B, tetracycline (TCL) displayed a higher reactivity towards PMS
424 molecule if compared to SMX. TCL displayed a complete degradation with the direct
425 reaction of PMS in 2 h. PDS and H_2O_2 did not oxidize the tetracycline molecule. The
426 kinetics of the reaction between TCL and PMS can be described as follows:

427 $$-\frac{dC_{TCL}}{dt} = k_{PMS,TCL} C_{PMS} C_{TCL} \quad (1)$$

428 where C_{TCL} and C_{PMS} are, respectively, the concentration of tetracycline and PMS, and
429 $k_{PMS,TCL}$ represents the second-order rate constant of the reaction. As PMS was in excess,
430 it can be considered that it is constant during the 2 h of reaction (C_{PMS}=0.5 mM),
431 simplifying Eq. (1) to a pseudo-first order kinetic expression. The pseudo-first order rate
432 constant during the direct reaction of PMS and TCL was 0.026±0.001 min^{-1}, leading to
433 value for $k_{PMS,TC}$=(3.4±0.1)·10^3 M^{-1} s^{-1}. Regarding adsorption removal, it was 80% in 2
434 h, as shown in Figure 7B. The combination of either PMS or PDS with MG0.2 led to the
435 complete elimination of tetracycline in 60 min.

Flumequine was the most recalcitrant organic to oxidation with the most limited adsorption removal, see Fig. 7C. No direct reaction was observed with none of the three inorganic oxidants. Flumequine has been reported to present no reactivity towards PMS [63] or PS unless temperature or pH is modified [64]. Adsorption led to only 30% of removal, reaching a plateau after the first 60 min. The addition of H_2O_2 or PDS barely improved the results already achieved during adsorption. However, the combination of PMS and MG0.2 significantly accelerated the elimination of flumequine (90% in 2h).

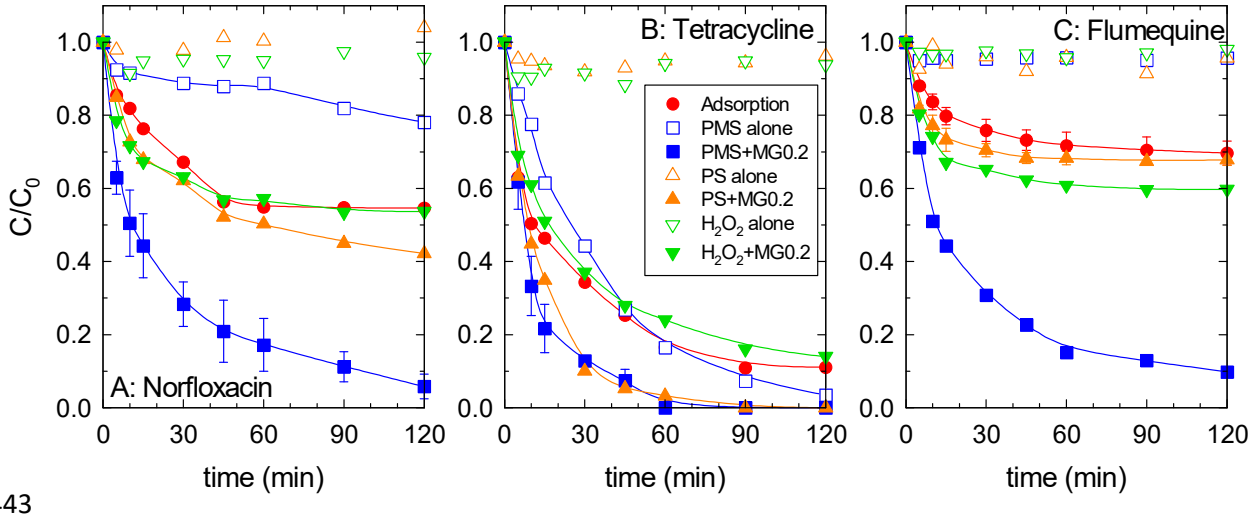

Figure 7. Removal of Norfloxacin (A), tetracycline (B) and flumequine (C) by activated inorganic peroxides with the magnetic graphene MG0.2. *Experimental conditions: V=250 mL; $C_{CEC,0}$= 5 mg L^{-1}; $C_{catalyst}$= 50 mg L^{-1}; $C_{oxidant}$=0.5 mM.*

3.3. Peroxymonosulfate activation with MG0.2 in simulated urban wastewater

To test the efficiency and behavior of the catalytic activation of peroxymonosulfate with MG0.2 in a more realistic scenario, different from ultrapure water, the degradation study of SMX was extended in a simulated urban wastewater (SUWW) matrix.

3.3.1. Concentration of the catalyst. Comparison of adsorption vs catalytic reaction

The influence of MG0.2 dose was first tested to compare the catalytic effect in the presence of PMS *versus* the adsorption process (PMS absence). Fig. 8 shows the evolution of SMX concentration in the SUWW matrix varying MG0.2 dose within 50-500 mg L^{-1}. It was observed that at 50 mg L^{-1} of MG0.2 dose, the SMX removal by adsorption was negligible in the SUWW matrix, due to the presence of organic matter in higher concentration than SMX that compete for active adsorption sites. An increase of MG0.2 dose led to higher adsorption removal as more active adsorption points on the surface were expected to be available. The addition PMS (0.5 mM) enhanced the final removal of SMX as well as the rate of the process in the entire catalyst dose tested. To analyze the effect of the catalyst dose on the efficiency of the process, the initial rate of SMX removal ($r_{SMX,0}$) was used as a tool. Fig. 8C depicts the estimated $r_{SMX,0}$ values of adsorption, and PMS catalysis processes. The $r_{SMX,0}$ in both processes is positively influenced by MG0.2 dose. The evolution of the ratio $r_{reac,0}/r_{ads,0}$ with the catalyst dose (Fig. 8C) indicates that the increase of MG0.2 enhanced the adsorption process to a higher extent than the PMS catalytic process.

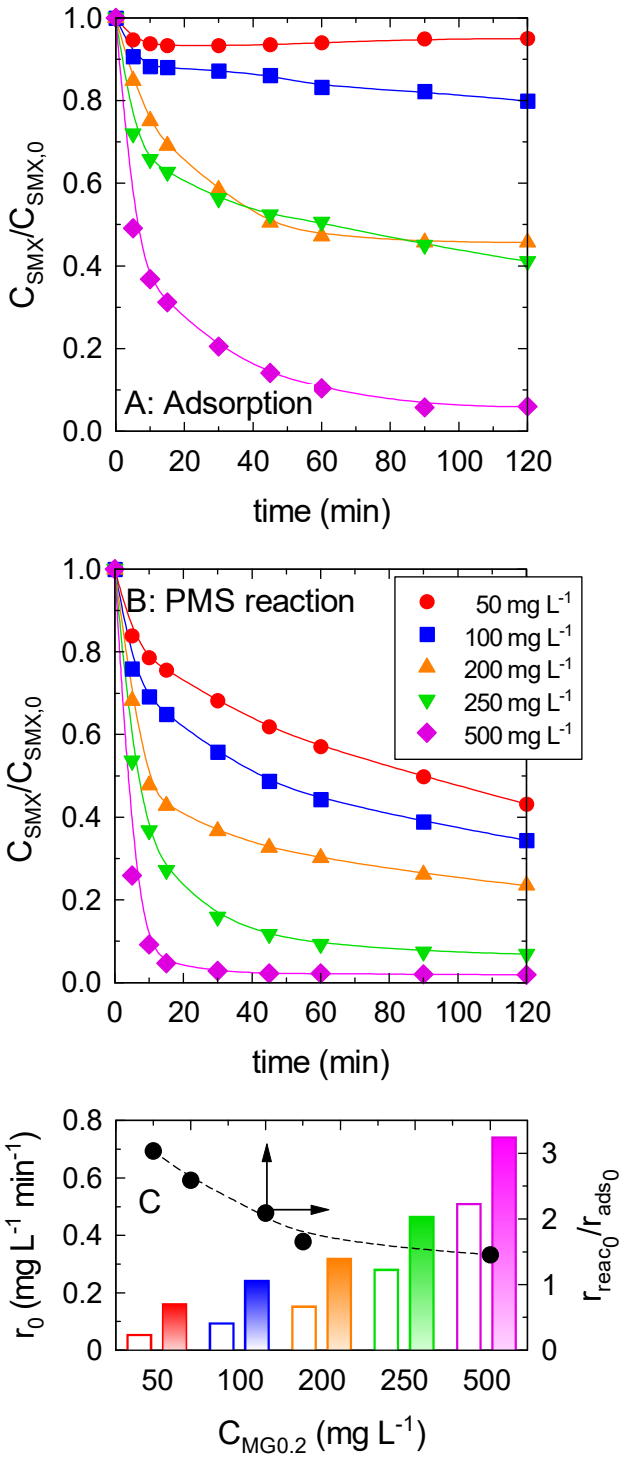

Figure 8. SMX removal in the SUWW matrix. Effect of MG0.2 dose in the adsorption (C) and PMS catalytic removal (B). Comparison of initial SMX removal rate of adsorption (empty bars) *vs* PMS activation (filled bars) with the catalyst MG0.2. *Experimental conditions: V=250 mL;* $C_{SMX,0}$*=5 mg* L^{-1}*;* $C_{PMS,0}$*=0.5 mM (if applied);* pH_i*=9.2±0.1*

3.3.2. The Initial concentration of peroxymonosulfate and sulfamethoxazole

The influence of initial PMS and SMX was assessed in the respective experimental series. The initial concentration of PMS was studied in a range of 0.10-10 mM. The evolution of SMX and the initial rate of SMX removal are depicted in Fig. 9A. The initial PMS concentration exerted a positive effect with an important increase of the initial SMX removal rate. Unlike the radical chemistry of PMS in which an overdose of PMS frequently affects negatively due to the auto-consumption of the unreacted PMS molecules with the radicals generated [65] to produce less active species; this behavior was not observed in this process. From the adjustment of $r_{SMX,0}$ with initial PMS concentration, it is observed an optimum of PMS dose (around 2-5 mM) after which the initial SMX rate keeps constant. Fig. 9B shows the influence of initial SMX concentration. The analysis of $r_{SMX,0}$ proved that the rate increased with the higher SMX amount in solution. Although from the evolution of this variable with initial SMX, a plateau can be envisaged, this behavior was out of the limit of the range studied (> 10 mg L^{-1}).

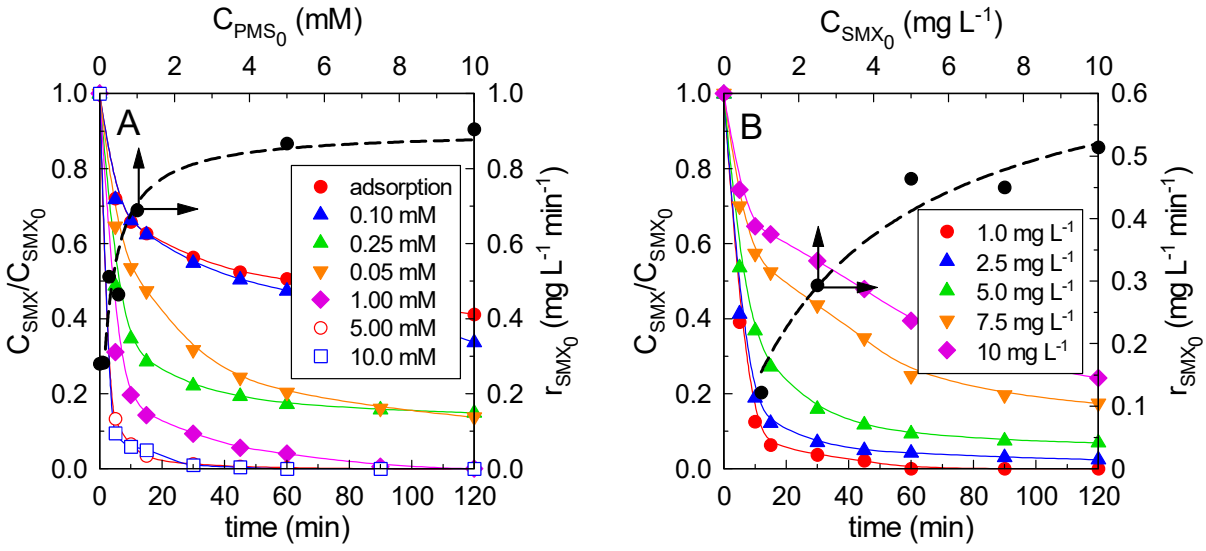

Figure 9. SMX removal in the SUWW matrix. Influence of initial PMS (A) and initial SMX concentration (B). *Experimental conditions: V=250 mL;* $C_{SMX,0}$*=5 mg* L^{-1}*;* $C_{MG0.2}$*=250 mg* L^{-1} *(A)* $C_{PMS,0}$*=0.5 mM (B);* pH_i*=9.2±0.1.*

491 *3.3.3. Effect of pH*

492 pH is an important variable to be studied in the design of technologies based on PMS.
493 The influence of pH has been studied within the range of 3-9. Due to the content of
494 inorganic salts that can buffer the pH in the SUWW matrix, only H_2SO_4 acid and NaOH
495 were added to adjust the pH to the desired value after PMS addition. Fig. 10A shows that
496 an increase of pH affected negatively the removal of SMX, especially at pH values up to
497 13. From the analysis of the evolution of the initial removal rate of SMX with pH and the
498 physical electrical interactions, it is expected a negative effect at a pH higher than the pK_a
499 of SMX. The pH_{pzc} of the catalyst MG0.2 was 4.83 (see Fig. 10B). This means that the
500 surface of the solid is positively charged at pH below 4.83, and negatively charged at
501 higher pH values. SMX molecule has two different pK_a values; it is protonated at pH
502 below 1.7, neutral within pH 1.7-5.7, and dissociated, that means negatively charged, at
503 pH>5.7 [66]. Therefore, electrostatic repulsions between SMX and MG0.2 surface are
504 expected at a pH higher than 5.7, which explains the negative effect registered during
505 SMX removal when raising the pH. This aspect must be taken into account for practical
506 design purposes of processes focused on wastewater since the pH of this wastewater
507 matrix is usually in the range of 7-8.

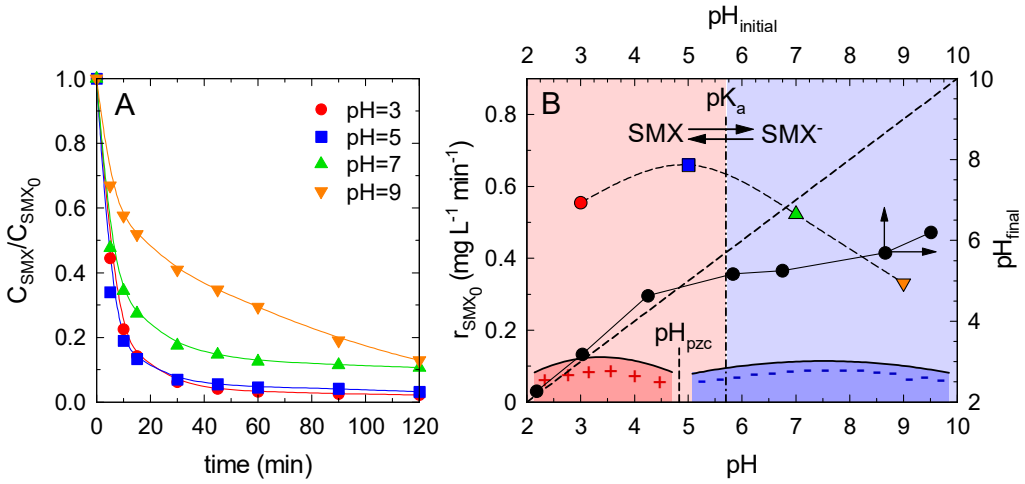

Figure 10. SMX removal in the SUWW matrix. Influence of pH in PMS catalytic activation. Evolution of normalized concentration of SMX (A). Evolution of initial removal rate of SMX *vs* pH and determination of the pH_{pzc} of MG0.2 (B). *Experimental conditions: V=250 mL; $C_{SMX,0}$=5 mg L^{-1}; $C_{MG0.2}$=250 mg L^{-1}; $C_{PMS,0}$=0.5 mM.*

3.3.4. Effect of water matrix

The effect of the influence of the matrix content was analyzed by carrying out different tests with more and less amount of the substances present in the matrix. These substances compete and/or block the pore/interstice for adsorption [67]. Moreover, there is expected competition for the reactive species generated from PMS catalytic decomposition. Fig. 11 depicts the effect of different concentrations of the SUWW matrix on SMX removal by the combination of MG0.2 and PMS. As can be observed, less efficient removal is appreciated, especially after doubling the concentration of the SUWW recipe. The presence of humic acid, bovine albumin, and sodium dodecyl-benzenesulfonate have been studied in the adsorption process of SMX in different carbon materials, including reduced graphene [68]. Dodecyl-benzenesulfonate exerted a higher inhibition if compared to the rest, which has been attributed to a higher size of this molecule. More importantly, HCO_3^- has been reported as an anion with one of the highest scavenging effect from the most common in water effluents, scavenging effect that is even higher than that of humic acid in the non-radical mediated mechanism of PMS activation [69]. However, the presence

528 of these substances, which compete with the micropollutant for adsorption and oxidation,
529 does not impose a considerable negative effect at the concentration levels they are in real
530 matrices and, therefore, they do not compromise the potential of this technology for real
531 applications [70]. Nevertheless, if the concentration of the organic matter is doubled or
532 higher (TOC higher than 22±1 mg L^{-1}), the feasibility of the technique is considerably
533 reduced. A practical solution would be an increase of the catalyst and/or PMS dose to
534 compensate for the matrix effect; however, the latter one would introduce more sulfate in
535 the solution.

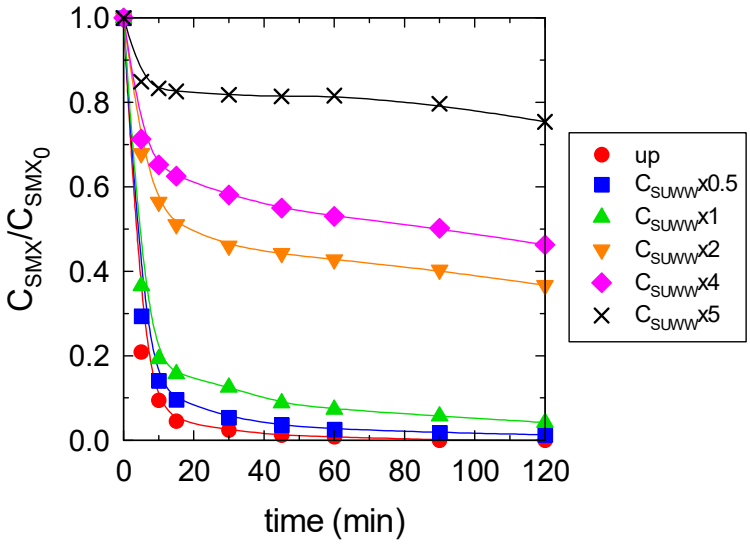

536

537 **Figure 11.** SMX removal in the SUWW matrix. Influence of SUWW concentration in
538 PMS catalytic activation. *Experimental conditions: V=250 mL;* $C_{SMX,0}$*=5 mg* L^{-1}*;*
539 $C_{MG0.2}$*=250 mg* L^{-1}*;* $C_{PMS,0}$*=0.5 mM;* pH_i*=9.2±0.1*

540 *3.3.5. Identification of the oxidative mechanism: scavengers and EPR studies*

541 It is hypothesized in carbonaceous materials that the peroxide bond in PMS can be
542 activated to generate singlet oxygen, through electron transfer from HSO_5^- molecule to
543 positively defective carbon sites in the surface of reduced graphene oxide (rGO) [71].
544 However, the oxidation role of $^1O_2$ seems to be debatable in detriment of electron transfer
545 reactions on the surface of the catalyst, especially under acidic conditions where the
546 production of $^1O_2$ is slower [72].

547 Fig. 12A depicts the results of the initial SMX removal in the presence of ethanol
548 (EtOH), tert-butyl alcohol (TBA), sodium azide, furfuryl alcohol (FFA), and L-Histidine
549 (L-H). Experiments have been carried out in ultrapure and SUWW matrix. EtOH and
550 TBA are good $HO^{\bullet}$ radical scavengers since both react fast, with a second-order rate
551 constant in the order of 10^9 and 10^8 M^{-1} s^{-1}, respectively. However, with sulfate radicals,
552 TBA presents 1000 magnitude less reactivity compared to $HO^{\bullet}$ while EtOH is 100 times
553 less reactive [8]. For that reason, the comparison of the efficiencies in the presence of EtOH
554 *vs* TBA can be used to differentiate the role played by sulfate radical and hydroxyl radical
555 [73]. Fig. 12A shows that EtOH and TBA did not influence the initial rate of SMX removal
556 either in ultrapure or in SUWW, which gives evidence about the lack of free radicals as
557 the main ROS involved in the process. Therefore, a combined contribution of radical and
558 non-radical pathways, as reported for catalytic activation of PMS based on metallic
559 catalysts [74], is dismissed.
560 To further evaluate the non-radical contribution, NaN_3, FFA, and L-H were tested
561 subsequently. NaN_3 and FFA are considered good quenchers for $^1O_2$ with the rate
562 constants of $1 \cdot 10^9$ and $1.2 \cdot 10^8$ M^{-1} s^{-1}, respectively. L-Histidine reacts with singlet oxygen
563 with a rate constant of $3 \cdot 10^7$ M^{-1} s^{-1}. These three scavengers are not completely selective
564 towards singlet oxygen as they also react with free radicals and even PMS [75]. As reported
565 in the literature[76], the consumption of PMS was accelerated in the presence of these
566 scavengers following the order NaN_3 > L-H > FFA (see Fig. S7). Therefore, the $^1O_2$
567 quenching effect cannot be entirely assumed. However, as the previous test with EtOH
568 and TBA indicated, the contribution of free radicals is negligible. Since $r_{SMX,0}$ is
569 considered as a tool for comparison purposes, the influence of the direct reaction of the
570 scavengers and PMS is minimized. The depletion of PMS during the first 5 min did not
571 reach in any case over 40%. At the concentration of scavengers used during the tests, 10

572 mM, NaN_3 and FFA led to partial inhibition but the process was not completely inhibited
573 if compared to adsorption. In this sense, L-Histidine led to better results. In the presence
574 of L-H, mostly all the reaction contribution was suppressed, reaching almost the same
575 initial SMX rate as observed during the adsorption process. These results indicate that the
576 oxidation of SMX may take place by non-radical activation of PMS. However, the
577 inhibition observed in r_{SXM0} is also due to the consumption of PMS by L-H, FFA, or
578 NaN_3. The contribution of singlet oxygen may be major, due to the alkaline pH value of
579 the SUWW matrix. Nevertheless, mediated electron-transfer reactions may also
580 contribute to the process as reported recently in similar studies of PMS activation with
581 carbonaceous materials [77].

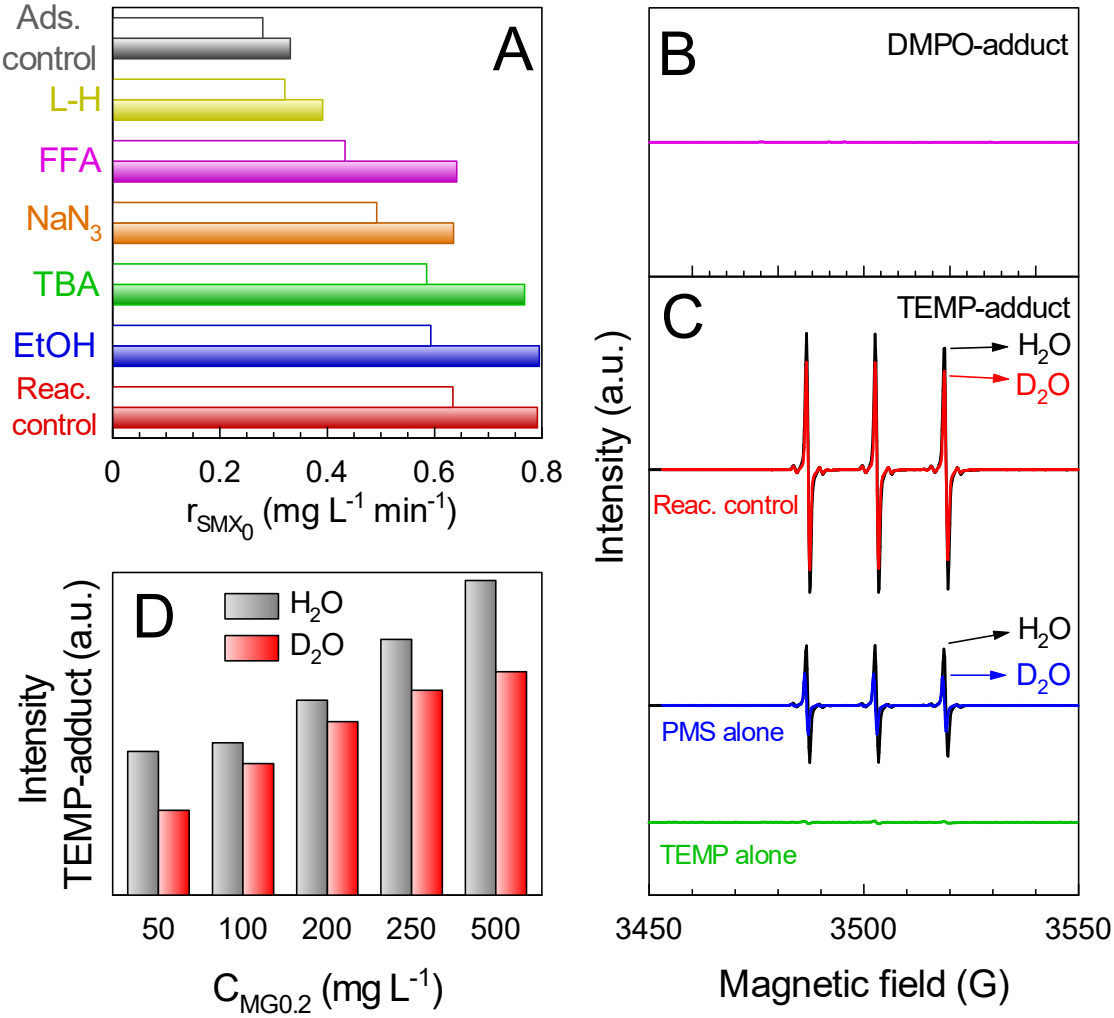

582

583 **Figure 12.** (A) Initial SMX removal rate in the presence of scavengers in ultrapure (filled
584 bars) and SUWW matrix (checkered bars) during PMS-catalytic activation. *Experimental*
585 *conditions: V=250 mL;* $C_{SMX,0}$*=5 mg* L^{-1}*;* $C_{MG0.2}$*=250 mg* L^{-1}*;* $C_{scavenger}$*= 10 mM;*
586 $C_{PMS,0}$*=0.5 mM;* pH_i*=9.2±0.1.* EPR spectra of PMS-catalytic activation using DMPO (B)
587 and TEMP (C) for singlet oxygen trapping. *Experimental conditions:* $C_{MG0.2}$*=250 mg* L^{-1}*;*
588 $C_{TEMP/DMPO}$*=0.1 M;* $C_{PMS,0}$*=0.5 mM;* pH_i*=9.2±0.1.* (D) EPR intensity of TEMP-adduct
589 during the activation of PMS with different doses of MG0.2. *Experimental conditions:*
590 $C_{MG0.2}$*=50-500 mg* L^{-1}*;* $C_{TEMP/DMPO}$*=0.1 M;* $C_{PMS,0}$*=0.5 mM;* pH_i*=9.2±0.1.*

591 Electron Paramagnetic Resonance (EPR) technique was used to corroborate the non-
592 radical activation of PMS and elucidate the nature of the process through singlet oxygen
593 formation or electron transfer mediated reaction. DMPO (5,5-dimethyl-1-pyrroline-N-
594 oxide) was used as trapping agent of radicals, e.g. hydroxyl radical, sulfate radical, and
595 superoxide [78]. Fig. 12B shows the EPR spectra of the aqueous solution with PMS, the
596 catalyst MG0.2, and DMPO. From the lack of peaks, it can be concluded that no
597 significant DMPO-OH, DMPO-SO_4, or DMPO-O_2 were generated in the PMS catalytic
598 activation, which supports the non-radical activation of PMS. In the presence of 4-amino-
599 2,2,6,6- tetramethylpiperidine (TEMP), a TEMP-adduct (named as TEMPO) was
600 detected, see Fig. 12C. The typical (1:1:1) triplet peak of the TEMPO was registered in
601 the absence of catalyst which is consistent with the activation of PMS in alkaline
602 conditions to release $^1O_2$ [79]. This triplet peak was gradually enlarged in the presence of
603 increasing doses of MG0.2 (see Fig. 12D). Although TEMPO nature in the absence of
604 catalyst is linked to the oxidation by singlet oxygen [79], there is debatable reasoning when
605 extrapolating it to the catalyzed systems, especially those involving carbonaceous
606 materials [72]. The occurrence of TEMPO in the EPR spectra is inconclusive evidence of
607 $^1O_2$ formation. TEMPO signal could also correspond to an electron-transfer reaction in
608 which the carbonaceous catalyst acts as an electron transfer mediator from TEMP to PMS,
609 leading to the formation of the $TEMP^{\bullet+}$ radical [80]. This $TEMP^{\bullet+}$ radical undergoes further

610 deprotonation and combination with dissolved oxygen to produce the observed TEMPO
611 signal. This alternative route can be confirmed with an EPR test of TEMP in the presence
612 of D_2O, an oxygenation enhancer. D_2O has been used as a strong evidence of singlet
613 oxygen presence due to the higher stability of $^1O_2$ in this deuterated medium.
614 Accordingly, $^1O_2$ may have been produced as consequence of electron transfer mediated
615 onto the surface of the material to trigger the formation of superoxide radical as reported
616 for Cu-rGO[69] or CuOMg-Fe_3O_4[81] heterostructures. The presence of superoxide radical
617 was negligible as suggested by the lack of a DMPO-adduct. Besides, if $^1O_2$ was produced
618 in the process, the TEMPO signal in the presence of D_2O should increase if compared to
619 the corresponding observed with H_2O. However, it was not the case. A decrease in the
620 signal was registered in all the tested catalyst doses. This fact provides evidence of
621 electron transfer from the organic TEMP to the PMS as responsible for the non-radical
622 oxidative route.

623 *3.3.6. Loss of activity in reusing cycles*

624 The loss of activity was evaluated by carrying out parallel sequential cycles of reaction
625 and adsorption of SMX in the real SUWW matrix. For comparison purposes, the tests in
626 ultrapure water were also completed. The solid was recovered with the help of a magnet
627 and dried overnight (100 °C). To balance the amount of solid lost during the filtration of
628 samples in each cycle and the thereafter recovery, the volume of solution was readjusted
629 after each test to meet the required initial catalyst concentration. Fig. 13 shows the
630 evolution of the initial SMX removal rate for adsorption and PMS-reaction in the
631 ultrapure water and SUWW matrix. In the case of ultrapure water, a stable behavior for
632 the catalyst in the presence of PMS was observed. Adsorption led to stable behavior but
633 in the fourth cycle is envisaged a partial loss due to the saturation of the surface with
634 SMX molecules. In the SUWW matrix, a loss in the activity for PMS-reaction was

observed during the two first cycles. After that the $r_{SMX,0}$ keeps constant after the third run. This behavior was also observed during adsorption in the SUWW matrix. The presence of diverse substances in the matrix that competes with SMX for active reaction sites on the surface may explain this behavior if results in ultrapure water and SUWW matrix are compared.

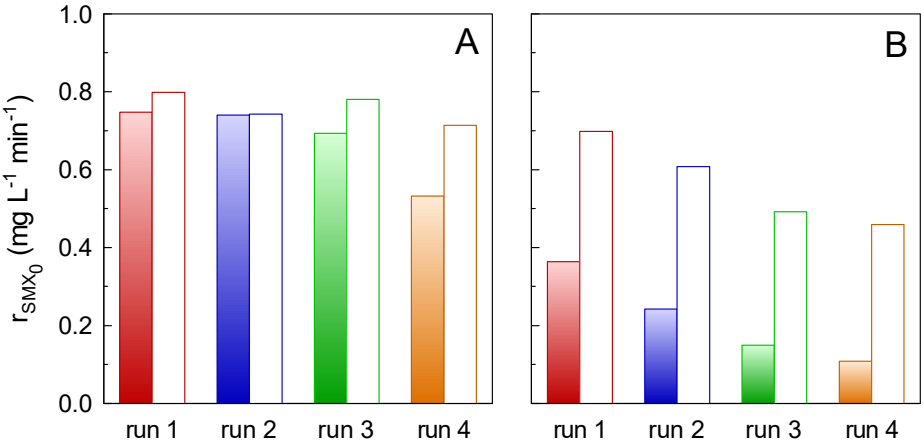

Figure 13. Deactivation of the MG0.2 catalyst in sequential reusing cycles of SMX removal in ultrapure water (A) and SUWW matrix (B). Evolution of the initial SMX reaction rate with recycling for adsorption (filled bars) and PMS-catalytic activation (checkered bars). Experimental conditions: V=250 mL; $C_{SMX,0}$=5 mg L^{-1}; $C_{PMS,0}$=0.5 mM; $C_{MG0.2}$=250 mg L^{-1}; pH_i=9.2±0.1

4. CONCLUSIONS

The incorporation of magnetite is an attractive strategy to synthesize magnetic graphene with application in water treatment. A stable and recoverable catalyst with low metal leaching was obtained in this study. Graphene exhibits higher catalytic activation of inorganic peroxides, especially peroxymonosulfate if compared to bare magnetite. Therefore, the proportion of magnetite should be designed according to the application under a magnetic field, raising the ratio of graphene in order not to compromise the catalytic activity. Magnetic graphene was efficient in the removal of antibiotics in ultrapure and wastewater depending on the nature of the organic. Those compounds with low adsorption removal and/or low reactivity towards PMS molecule, i.e. norfloxacin and

656 flumequine, showed the best improvements when the simultaneous application of PMS
657 and magnetic graphene was applied. Moderate improvements on the reaction rate were
658 found in sulfamethoxazole and to less extent in flumequine, due to their reactivity towards
659 PMS molecule or affinity towards adsorption on the solid. In wastewater, it was necessary
660 to increase five or even ten times the catalyst dose to reach similar percentage degradation
661 rates of the target compound due to the competition with other substances in the
662 background for adsorption onto active sites. The initial dose of PMS after an optimum
663 value did not affect substantially the efficiency in the process. pH values around 5 showed
664 the best performance on the removal of antibiotics. From the scavenger study, a non-
665 radical activation of peroxymonosulfate may be hypothesized. EPR technique not only
666 provided evidence to affirm the occurrence of the hypothesized non-radical mechanism
667 but also to elucidate that this non-radical mechanism takes place *via* electron-transfer
668 reaction from the organic to PMS onto the surface of the graphene-based material,
669 discharging the formation of $^1O_2$. The catalyst performance was completely stable in
670 ultrapure water after recycling while a slight decrease during the first runs was registered
671 in the wastewater. The heterojunction of magnetite nanoparticles and graphene is a
672 feasible strategy for the catalytic activation of inorganic peroxides and its application in
673 the treatment of aqueous organic micropollutants. This strategy, however, involves the
674 addition of peroxymonosulfate in water whose presence may be limited or be negative
675 depending on the further use of wastewater.

676 **Acknowledgments**

677 Rafael Rodríguez Solís is grateful to *Ramón Areces Foundation* (Madrid, Spain) for
678 his postdoctoral fellowship at the University of Cincinnati (XXX edition of grants for
679 Postgraduate Studies in Life and Matter Sciences in Foreign Universities and Research
680 Centers 2018/2019). Özge Dinc acknowledges the 2219-TUBITAK International Post-

Doctoral Research Fellowship Program. Dr. Guodong Fang acknowledges the grant from the National Natural Science Foundation of China (42022049). D. D. Dionysiou acknowledges support from the University of Cincinnati through a UNESCO co-Chair Professor position on “Water Access and Sustainability” and the Herman Schneider Professorship in the College of Engineering and Applied Sciences.

The research presented was not performed by or funded by EPA and was not subject to EPA's quality system requirements. Consequently, the views, interpretations, and conclusions expressed in this article are solely those of the authors and do not necessarily reflect or represent EPA's views or policies.

Authors would like to express their gratitude for the help with the analysis of magnetic graphene samples to the following facilities: The *Advanced Materials Characterization Center* and *Chemical Sensors and Biosensors* of the University of Cincinnati (Cincinnati, OH, USA), the *Chemical Sensors and Biosensors* of the University of Notre Dame (Notre Dame, IN, USA), the *Cornell Center for Materials Research* (NSF award number DMR-1719875) of the Cornell University (Ithaca, NY, USA).

REFERENCES

1 A. Gogoi, P. Mazumder, V. K. Tyagi, G. G. Tushara Chaminda, A. K. An and M. Kumar, Occurrence and fate of emerging contaminants in water environment: A review, *Groundw. Sustain. Dev.*, 2018, **6**, 169–180.

2 I. Michael, L. Rizzo, C. S. McArdell, C. M. Manaia, C. Merlin, T. Schwartz, C. Dagot and D. Fatta-Kassinos, Urban wastewater treatment plants as hotspots for the release of antibiotics in the environment: A review, *Water Res.*, 2013, **47**, 957–995.

3 E. Nilsen, K. L. Smalling, L. Ahrens, M. Gros, K. S. B. Miglioranza, Y. Picó and H. L. Schoenfuss, Critical review: Grand challenges in assessing the adverse

706 effects of contaminants of emerging concern on aquatic food webs, *Environ.*
707 *Toxicol. Chem.*, 2019, **38**, 46–60.
708 4 A. R. Lado Ribeiro, N. F. F. Moreira, G. Li Puma and A. M. T. Silva, Impact of
709 water matrix on the removal of micropollutants by advanced oxidation
710 technologies, *Chem. Eng. J.*, 2019, **363**, 155–173.
711 5 L. Rizzo, T. Agovino, S. Nahim-Granados, M. Castro-Alférez, P. Fernández-
712 Ibáñez and M. I. Polo-López, Tertiary treatment of urban wastewater by solar and
713 UV-C driven advanced oxidation with peracetic acid: Effect on contaminants of
714 emerging concern and antibiotic resistance, *Water Res.*, 2019, **149**, 272–281.
715 6 S. Chen, M. Cai, Y. Liu, L. Zhang and L. Feng, Effects of water matrices on the
716 degradation of naproxen by reactive radicals in the UV/peracetic acid process,
717 *Water Res.*, 2019, **150**, 153–161.
718 7 Y. Huang, M. Kong, D. Westerman, E. G. Xu, S. Coffin, K. H. Cochran, Y. Liu,
719 S. D. Richardson, D. Schlenk and D. D. Dionysiou, Effects of HCO_3^- on
720 Degradation of Toxic Contaminants of Emerging Concern by UV/NO_3^-, *Environ.*
721 *Sci. Technol.*, 2018, **52**, 12697–12707.
722 8 S. Wacławek, H. V. Lutze, K. Grübel, V. V. T. Padil, M. Černík and D. D.
723 Dionysiou, Chemistry of persulfates in water and wastewater treatment: A review,
724 *Chem. Eng. J.*, 2017, **330**, 44–62.
725 9 W.-D. Oh, Z. Dong and T.-T. Lim, Generation of sulfate radical through
726 heterogeneous catalysis for organic contaminants removal: Current development,
727 challenges and prospects, *Appl. Catal. B Environ.*, 2016, **194**, 169–201.
728 10 J. Wang and S. Wang, Activation of persulfate (PS) and peroxymonosulfate (PMS)
729 and application for the degradation of emerging contaminants, *Chem. Eng. J.*,
730 2018, **334**, 1502–1517.

11 R. Xiao, Z. Luo, Z. Wei, S. Luo, R. Spinney, W. Yang and D. D. Dionysiou, Activation of peroxymonosulfate/persulfate by nanomaterials for sulfate radical-based advanced oxidation technologies, *Curr. Opin. Chem. Eng.*, 2018, **19**, 51–58.

12 S. Chowdhury and R. Balasubramanian, Recent advances in the use of graphene-family nanoadsorbents for removal of toxic pollutants from wastewater, *Adv. Colloid Interface Sci.*, 2014, **204**, 35–56.

13 G. Ersan, O. G. Apul, F. Perreault and T. Karanfil, Adsorption of organic contaminants by graphene nanosheets: A review, *Water Res.*, 2017, **126**, 385–398.

14 S. Indrawirawan, H. Sun, X. Duan and S. Wang, Nanocarbons in different structural dimensions (0–3D) for phenol adsorption and metal-free catalytic oxidation, *Appl. Catal. B Environ.*, 2015, **179**, 352–362.

15 X. Chen, W.-D. Oh and T.-T. Lim, Graphene- and CNTs-based carbocatalysts in persulfates activation: Material design and catalytic mechanisms, *Chem. Eng. J.*, 2018, **354**, 941–976.

16 M. N. Chong, B. Jin, C. W. K. Chow and C. Saint, Recent developments in photocatalytic water treatment technology: A review, *Water Res.*, 2010, **44**, 2997–3027.

17 B. Srikanth, R. Goutham, R. Badri Narayan, A. Ramprasath, K. P. Gopinath and A. R. Sankaranarayanan, Recent advancements in supporting materials for immobilised photocatalytic applications in waste water treatment, *J. Environ. Manage.*, 2017, **200**, 60–78.

18 P. Xu, G. M. Zeng, D. L. Huang, C. L. Feng, S. Hu, M. H. Zhao, C. Lai, Z. Wei, C. Huang, G. X. Xie and Z. F. Liu, Use of iron oxide nanomaterials in wastewater treatment: A review, *Sci. Total Environ.*, 2012, **424**, 1–10.

19 S. K. Sahoo, S. Padhiari, S. K. Biswal, B. B. Panda and G. Hota, Fe3O4

nanoparticles functionalized GO/g-C_3N_4 nanocomposite: An efficient magnetic nanoadsorbent for adsorptive removal of organic pollutants, *Mater. Chem. Phys.*, 2020, **244**, 122710.

20 W. Wang, Y. Cao, X. Hu, S. Zhou, D. Zhu, D. Qi and S. Deng, Granular reduced graphene oxide/Fe3O4 hydrogel for efficient adsorption and catalytic oxidation of p-perfluorous nonenoxybenzene sulfonate, *J. Hazard. Mater.*, 2020, **386**, 121662.

21 Y. Pang, Y. Zhou, K. Luo, Z. Zhang, R. Yue, X. Li and M. Lei, Activation of persulfate by stability-enhanced magnetic graphene oxide for the removal of 2,4-dichlorophenol, *Sci. Total Environ.*, 2020, **707**, 135656.

22 M. N. Pervez, W. He, T. Zarra, V. Naddeo and Y. Zhao, New Sustainable Approach for the Production of Fe_3O_4/Graphene Oxide-Activated Persulfate System for Dye Removal in Real Wastewater, *Water*, 2020, **12**, 733.

23 D. E. Santiago, L. M. Pastrana-Martínez, E. Pulido-Melián, J. Araña, J. L. Faria, A. M. T. Silva, Ó. González-Díaz and J. M. Doña-Rodríguez, TiO_2-based (Fe_3O_4, SiO_2, reduced graphene oxide) magnetically recoverable photocatalysts for imazalil degradation in a synthetic wastewater, *Environ. Sci. Pollut. Res.*, 2018, **25**, 27724–27736.

24 A. M. Chávez, R. R. Solís and F. J. Beltrán, Magnetic graphene TiO_2-based photocatalyst for the removal of pollutants of emerging concern in water by simulated sunlight aided photocatalytic ozonation, *Appl. Catal. B Environ.*, 2020, **262**, 118275.

25 Z. Q. Li, H. L. Wang, L. Y. Zi, J. J. Zhang and Y. S. Zhang, Preparation and photocatalytic performance of magnetic TiO_2–Fe_3O_4/graphene (RGO) composites under VIS-light irradiation, *Ceram. Int.*, 2015, **41**, 10634–10643.

26 L. Erdei, N. Arecrachakul and S. Vigneswaran, A combined photocatalytic slurry

reactor–immersed membrane module system for advanced wastewater treatment, *Sep. Purif. Technol.*, 2008, **62**, 382–388.

27 S. Gokulakrishnan, A. Mohammed and H. Prakash, Determination of persulphates using N,N-diethyl-p-phenylenediamine as colorimetric reagent: Oxidative coloration and degradation of the reagent without bactericidal effect in water, *Chem. Eng. J.*, 2016, **286**, 223–231.

28 G. Eisenberg, Colorimetric Determination of Hydrogen Peroxide, *Ind. Eng. Chem. Anal. Ed.*, 1943, **15**, 327–328.

29 M. Cao, P. Wang, Y. Ao, C. Wang, J. Hou and J. Qian, Photocatalytic degradation of tetrabromobisphenol A by a magnetically separable graphene–TiO_2 composite photocatalyst: Mechanism and intermediates analysis, *Chem. Eng. J.*, 2015, **264**, 113–124.

30 K. Petcharoen and A. Sirivat, Synthesis and characterization of magnetite nanoparticles via the chemical co-precipitation method, *Mater. Sci. Eng. B*, 2012, **177**, 421–427.

31 R. Valenzuela, M. C. Fuentes, C. Parra, J. Baeza, N. Duran, S. K. Sharma, M. Knobel and J. Freer, Influence of stirring velocity on the synthesis of magnetite nanoparticles (Fe_3O_4) by the co-precipitation method, *J. Alloys Compd.*, 2009, **488**, 227–231.

32 G. Liu, H. Yu, N. Wang, R. Jin, J. Wang and J. Zhou, Microbial reduction of Ferrihydrite in the presence of reduced Graphene oxide materials: Alteration of Fe(III) reduction rate, biomineralization product and settling behavior, *Chem. Geol.*, 2018, **476**, 272–279.

33 L. M. Malard, M. A. Pimenta, G. Dresselhaus and M. S. Dresselhaus, *Phys. Rep.*, 2009, 473, 51–87.

806 34 C. Bartlam, S. Morsch, K. W. J. Heard, P. Quayle, S. G. Yeates and A.
807 Vijayaraghavan, Nanoscale infrared identification and mapping of chemical
808 functional groups on graphene, *Carbon N. Y.*, 2018, **139**, 317–324.
809 35 A. A. K. King, B. R. Davies, N. Noorbehesht, P. Newman, T. L. Church, A. T.
810 Harris, J. M. Razal and A. I. Minett, A new Raman metric for the characterisation
811 of graphene oxide and its derivatives, *Sci. Rep.*, 2016, **6**, 1–6.
812 36 A. Eckmann, A. Felten, A. Mishchenko, L. Britnell, R. Krupke, K. S. Novoselov
813 and C. Casiraghi, Probing the nature of defects in graphene by Raman
814 spectroscopy, *Nano Lett.*, 2012, **12**, 3925–3930.
815 37 J. Zhou, H. Song, L. Ma and X. Chen, Magnetite/graphene nanosheet composites:
816 interfacial interaction and its impact on the durable high-rate performance in
817 lithium-ion batteries, *RSC Adv.*, 2011, **1**, 782–791.
818 38 S. Qilong, S. Lei, C. Yingying, Y. Wei, X. Sijun, J. Tao and Y. Guoqiu, Fe_3O_4-
819 intercalated reduced graphene oxide nanocomposites with enhanced microwave
820 absorption properties, *Ceram. Int.*, 2019, **45**, 18298–18305.
821 39 A. P. Grosvenor, B. A. Kobe, M. C. Biesinger and N. S. McIntyre, Investigation
822 of multiplet splitting of Fe 2p XPS spectra and bonding in iron compounds, *Surf.*
823 *Interface Anal.*, 2004, **36**, 1564–1574.
824 40 R. L. Rebodos and P. J. Vikesland, Effects of oxidation on the magnetization of
825 nanoparticulate magnetite, *Langmuir*, 2010, **26**, 16745–16753.
826 41 S. J. Kemp, R. M. Ferguson, A. P. Khandhar and K. M. Krishnan, Monodisperse
827 magnetite nanoparticles with nearly ideal saturation magnetization, *RSC Adv.*,
828 2016, **6**, 77452–77464.
829 42 A. Rey, D. H. Quiñones, P. M. Álvarez, F. J. Beltrán and P. K. Plucinski, Simulated
830 solar-light assisted photocatalytic ozonation of metoprolol over titania-coated

magnetic activated carbon, *Appl. Catal. B Environ.*, 2012, **111**–**112**, 246–253.

43 D. H. Quiñones, A. Rey, P. M. Álvarez, F. J. Beltrán and P. K. Plucinski, Enhanced activity and reusability of TiO_2 loaded magnetic activated carbon for solar photocatalytic ozonation, *Appl. Catal. B Environ.*, 2014, **144**, 96–106.

44 H. C. Vu, A. D. Dwivedi, T. T. Le, S. H. Seo, E. J. Kim and Y. S. Chang, Magnetite graphene oxide encapsulated in alginate beads for enhanced adsorption of Cr(VI) and As(V) from aqueous solutions: Role of crosslinking metal cations in pH control, *Chem. Eng. J.*, 2017, **307**, 220–229.

45 T. Liu, D. Zhang, K. Yin, C. Yang, S. Luo and J. C. Crittenden, Degradation of thiacloprid via unactivated peroxymonosulfate: The overlooked singlet oxygen oxidation, *Chem. Eng. J.*, 2020, **388**, 124264.

46 R. Yin, W. Guo, H. Wang, J. Du, X. Zhou, Q. Wu, H. Zheng, J. Chang and N. Ren, Selective degradation of sulfonamide antibiotics by peroxymonosulfate alone: Direct oxidation and nonradical mechanisms, *Chem. Eng. J.*, 2018, **334**, 2539–2546.

47 Y. Ji, J. Lu, L. Wang, M. Jiang, Y. Yang, P. Yang, L. Zhou, C. Ferronato and J.-M. Chovelon, Non-activated peroxymonosulfate oxidation of sulfonamide antibiotics in water: Kinetics, mechanisms, and implications for water treatment, *Water Res.*, 2018, **147**, 82–90.

48 W. Peng, S. Liu, H. Sun, Y. Yao, L. Zhi and S. Wang, Synthesis of porous reduced graphene oxide as metal-free carbon for adsorption and catalytic oxidation of organics in water, *J. Mater. Chem. A*, 2013, **1**, 5854–5859.

49 N. A. Zubir, C. Yacou, J. Motuzas, X. Zhang and J. C. Diniz Da Costa, Structural and functional investigation of graphene oxide-Fe_3O_4 nanocomposites for the heterogeneous Fenton-like reaction, *Sci. Rep.*, 2014, **4**, 4594.

50 Y. Hua, S. Wang, J. Xiao, C. Cui and C. Wang, Preparation and characterization of Fe_3O_4/gallic acid/graphene oxide magnetic nanocomposites as highly efficient Fenton catalysts, *RSC Adv.*, 2017, **7**, 28979–28986.

51 J. Yan, W. Gao, M. Dong, L. Han, L. Qian, C. P. Nathanail and M. Chen, Degradation of trichloroethylene by activated persulfate using a reduced graphene oxide supported magnetite nanoparticle, *Chem. Eng. J.*, 2016, **295**, 309–316.

52 L. Xu and J. Wang, Fenton-like degradation of 2,4-dichlorophenol using Fe_3O_4 magnetic nanoparticles, *Appl. Catal. B Environ.*, 2012, **123**–**124**, 117–126.

53 G.-D. Fang, D. D. Dionysiou, S. R. Al-Abed and D.-M. Zhou, Superoxide radical driving the activation of persulfate by magnetite nanoparticles: Implications for the degradation of PCBs, *Appl. Catal. B Environ.*, 2013, **129**, 325–332.

54 A. Hassani, M. Karaca, S. Karaca, A. Khataee, Ö. Açışlı and B. Yılmaz, Preparation of magnetite nanoparticles by high-energy planetary ball mill and its application for ciprofloxacin degradation through heterogeneous Fenton process, *J. Environ. Manage.*, 2018, **211**, 53–62.

55 L. Hou, Q. Zhang, F. Jérôme, D. Duprez, H. Zhang and S. Royer, Shape-controlled nanostructured magnetite-type materials as highly efficient Fenton catalysts, *Appl. Catal. B Environ.*, 2014, **144**, 739–749.

56 R. Matta, K. Hanna and S. Chiron, Fenton-like oxidation of 2,4,6-trinitrotoluene using different iron minerals, *Sci. Total Environ.*, 2007, **385**, 242–251.

57 L. Hou, H. Zhang and X. Xue, Ultrasound enhanced heterogeneous activation of peroxydisulfate by magnetite catalyst for the degradation of tetracycline in water, *Sep. Purif. Technol.*, 2012, **84**, 147–152.

58 M. Usman, P. Faure, C. Ruby and K. Hanna, Application of magnetite-activated persulfate oxidation for the degradation of PAHs in contaminated soils,

Chemosphere, 2012, **87**, 234–240.

59 D. Ding, C. Liu, Y. Ji, Q. Yang, L. Chen, C. Jiang and T. Cai, Mechanism insight of degradation of norfloxacin by magnetite nanoparticles activated persulfate: Identification of radicals and degradation pathway, *Chem. Eng. J.*, 2017, **308**, 330–339.

60 C. Tan, N. Gao, Y. Deng, J. Deng, S. Zhou, J. Li and X. Xin, Radical induced degradation of acetaminophen with Fe_3O_4 magnetic nanoparticles as heterogeneous activator of peroxymonosulfate, *J. Hazard. Mater.*, 2014, **276**, 452–460.

61 E. Saputra, S. Muhammad, H. Sun, H.-M. Ang, M. O. Tadé and S. Wang, A comparative study of spinel structured Mn_3O_4, Co_3O_4 and Fe_3O_4 nanoparticles in catalytic oxidation of phenolic contaminants in aqueous solutions, *J. Colloid Interface Sci.*, 2013, **407**, 467–473.

62 X. Duan, H. Sun, Z. Shao and S. Wang, Nonradical reactions in environmental remediation processes: Uncertainty and challenges, *Appl. Catal. B Environ.*, 2018, **224**, 973–982.

63 M. Nihemaiti, R. R. Permala and J. P. Croué, Reactivity of unactivated peroxymonosulfate with nitrogenous compounds, *Water Res.*, 2020, **169**, 115221.

64 M. Feng, R. Qu, X. Zhang, P. Sun, Y. Sui, L. Wang and Z. Wang, Degradation of flumequine in aqueous solution by persulfate activated with common methods and polyhydroquinone-coated magnetite/multi-walled carbon nanotubes catalysts, *Water Res.*, 2015, **85**, 1–10.

65 S. K. Ling, S. Wang and Y. Peng, Oxidative degradation of dyes in water using Co^{2+}/H_2O_2 and Co^{2+}/peroxymonosulfate, *J. Hazard. Mater.*, 2010, **178**, 385–389.

66 A. L. Boreen, A. William A. Arnold and K. McNeill, Photochemical Fate of Sulfa

906 Drugs in the Aquatic Environment: Sulfa Drugs Containing Five-Membered
907 Heterocyclic Groups, *Environ. Sci. Technol*, 2004, **38**, 3933–3940.
908 67 G. Ersan, Y. Kaya, O. G. Apul and T. Karanfil, Adsorption of organic contaminants
909 by graphene nanosheets, carbon nanotubes and granular activated carbons under
910 natural organic matter preloading conditions, *Sci. Total Environ.*, 2016, **565**, 811–
911 817.
912 68 F.-F. Liu, J. Zhao, S. Wang and B. Xing, Adsorption of sulfonamides on reduced
913 graphene oxides as affected by pH and dissolved organic matter, *Environ. Pollut.*,
914 2016, **210**, 85–93.
915 69 A. Shahzad, J. Ali, J. Ifthikar, G. G. Aregay, J. Zhu, Z. Chen and Z. Chen, Non-
916 radical PMS activation by the nanohybrid material with periodic confinement of
917 reduced graphene oxide (rGO) and Cu hydroxides, *J. Hazard. Mater.*, 2020, **392**,
918 122316.
919 70 A. Khan, J. Wang, J. Li, X. Wang, Z. Chen, A. Alsaedi, T. Hayat, Y. Chen and X.
920 Wang, The role of graphene oxide and graphene oxide-based nanomaterials in the
921 removal of pharmaceuticals from aqueous media: a review, *Environ. Sci. Pollut.*
922 *Res.*, 2017, **24**, 7938–7958.
923 71 P. Sun, H. Liu, M. Feng, L. Guo, Z. Zhai, Y. Fang, X. Zhang and V. K. Sharma,
924 Nitrogen-sulfur co-doped industrial graphene as an efficient peroxymonosulfate
925 activator: Singlet oxygen-dominated catalytic degradation of organic
926 contaminants, *Appl. Catal. B Environ.*, 2019, **251**, 335–345.
927 72 J. Lee, U. von Gunten and J.-H. Kim, Persulfate-based Advanced Oxidation:
928 Critical Assessment of Opportunities and Roadblocks, *Environ. Sci. Technol.*,
929 2020, **54**, 3064–3081.
930 73 F. Ghanbari and M. Moradi, Application of peroxymonosulfate and its activation

methods for degradation of environmental organic pollutants: Review, *Chem. Eng. J.*, 2017, **310**, 41–62.

74 X. Zhou, C. Luo, M. Luo, Q. Wang, J. Wang, Z. Liao, Z. Chen and Z. Chen, Understanding the synergetic effect from foreign metals in bimetallic oxides for PMS activation: A common strategy to increase the stoichiometric efficiency of oxidants, *Chem. Eng. J.*, 2020, **381**, 122587.

75 Y. Yang, G. Banerjee, G. W. Brudvig, J.-H. Kim and J. J. Pignatello, Oxidation of Organic Compounds in Water by Unactivated Peroxymonosulfate, *Environ. Sci. Technol.*, 2018, **52**, 5911–5919.

76 S. Zhu, X. Li, J. Kang, X. Duan and S. Wang, Persulfate Activation on Crystallographic Manganese Oxides: Mechanism of Singlet Oxygen Evolution for Nonradical Selective Degradation of Aqueous Contaminants, *Environ. Sci. Technol.*, 2019, **53**, 307–315.

77 E. T. Yun, J. H. Lee, J. Kim, H. D. Park and J. Lee, Identifying the Nonradical Mechanism in the Peroxymonosulfate Activation Process: Singlet Oxygenation Versus Mediated Electron Transfer, *Environ. Sci. Technol.*, 2018, **52**, 7032–7042.

78 G. Fang, J. Gao, D. D. Dionysiou, C. Liu and D. Zhou, Activation of persulfate by quinones: Free radical reactions and implication for the degradation of PCBs, *Environ. Sci. Technol.*, 2013, **47**, 4605–4611.

79 C. Qi, X. Liu, J. Ma, C. Lin, X. Li and H. Zhang, Activation of peroxymonosulfate by base: Implications for the degradation of organic pollutants, *Chemosphere*, 2016, **151**, 280–288.

80 G. Nardi, I. Manet, S. Monti, M. A. Miranda and V. Lhiaubet-Vallet, Scope and limitations of the TEMPO/EPR method for singlet oxygen detection: The misleading role of electron transfer, *Free Radic. Biol. Med.*, 2014, **77**, 64–70.

81 A. Jawad, K. Zhan, H. Wang, A. Shahzad, Z. Zeng, J. Wang, X. Zhou, H. Ullah, Z. Chen and Z. Chen, Tuning of Persulfate Activation from a Free Radical to a Nonradical Pathway through the Incorporation of Non-Redox Magnesium Oxide, *Environ. Sci. Technol*, 2020, **54**, 2476–2488.